3-D SIMULATION OF DROPLET IMPACT ON STATIC AND MOVING WALLS

A Thesis

by

Anıl Yılmaz

Submitted to the
Graduate School of Sciences and Engineering
In Partial Fulfillment of the Requirements for
the Degree of

Master of Science

in the
Department of Mechanical Engineering

Özyeğin University
January 2021

3-D SIMULATION OF DROPLET IMPACT ON STATIC AND MOVING WALLS

Approved by:

Asst. Prof. Dr.-Ing Özgür Ertunç, Advisor
Department of Mechanical Engineering
Özyeğin University

Asst. Prof. Dr. Altuğ Melik Başol
Department of Mechanical Engineering
Özyeğin University

Assoc.Prof. Dr. Ayşe Gül Güngör
Department of Astronautical Engineering
Istanbul Tecnical University

Date Approved: 13 January 2021

To my family

ABSTRACT

In the present study, the contact angle model and origin of the parasitic current have been studied to provide accurate prediction of droplet surface interactions in Volume of Fluid (VOF) framework. We investigate the effect of “modelled” dynamic contact angle boundary conditions to 3D droplet spread&deposition size and the parasitic currents relation with grid distribution. According the simulation experience, OpenFOAM’s static and classical dynamic contact angle calculations are insufficient to provide accurate droplet spread and deposition ratio. In fact, it was shown that the classical Kistler dynamic contact angle model did not perform well in low capillary numbers and in cases where the difference in advancing and receding angles was high. It has been possible to reduce the unphysical flow problem seen in the interface region in multiphase simulations with structural changes. It has been quantitatively shown that the number of neighboring cells sharing the same faces influences the gradient calculations associated with the formation of parasitic current. It has been observed that the polyhedral cell structure delivers smoother the interface gradient distribution than the cartesian cell structure. After implementing, modified Kistler contact angle model in OpenFoam and using polyhedral cells for the simulations, we could succesfully validate transient droplet shapes formed upon impact with those obtained from experiments. Droplet outcomes, such as deposition, partial rebound and split deposition on stationary and moving smooth surfaces are obtained consistent with experimental results..

ÖZETÇE

Bu çalışmada, damlacık-yüzey etkileşimlerinin VOF method çalışma düzleminde analizinin yapılabilmesi için kontak açısı modeli ve parazitik akımların kaynağı üzerine çalışmalar yapılmıştır. Modellenmiş dinamik kontak açısı sınır koşulunun 3 boyutlu damlacık yayılma ve toparlanma boyutlarına ve grid dağılımının parazitik akımlar üzerine etkisi incelenmiştir. Daha önceki simülasyon deneyimlerimize göre, OpenFOAM'un statik ve klasik dinamik kontak açısı modelleri, damlanın yayılma ve toparlanma çaplarının oranın hesaplanması noktasında yetersiz kaldığı görülmüştür. Aslında Kistler dinamik kontak açısı modeli de düşük damlacık hızlarında ve yayılma ve toparlanma açılarının farkının yüksek olduğu durumlarda iyi performans göstermediği bu çalışmada gösterilmiştir. Çok fazlı akış simulasyonlarında yapısal değişikliklerle arayüz üzerindeki fiziksel olmayan akış durumları engellenebilmektedir. Merkezi hacmin komşu kenar sayısı ve hacmin şeklinin parazitik akımların formunu etkilediği modellenerek gösterilmiştir. Bu modellemelerden, polyhedral hücre yapısının kartezyen hücre yapısına sahip simulasyonlara karşı arayüz gradient hesaplamalarında daha iyi dağılım gösterdiği anlaşılmıştır. Polyhderal mesh tipinin uygulanması ve Kistler kontak açısı modelinin modifiye edilmesinden sonra OpenFoam ile yapılan simulasyonların deneysel sonuçlar ile eşleşmesi başarı ile gerçekleşmiştir . Burada damla simülasyonlarının sonuçlarını (deposition, partial rebound and split deposition) hareketli ve durağan pürüzsüz yüzeylerdeki deneysel sonuçlar ile eşleştirmesini gösterdik.

ACKNOWLEDGEMENTS

I would like to kindly acknowledge my supervisor Asst. Prof.Dr. Özgür Ertunç for his contributions to me and my work. I would like to thank him for his work discipline, unexpected questions, mathematical and physical knowledge, and for being generous in providing all the necessary opportunities for a study to his students, for his great efforts in my development and this work.I would also like to thank Gökhan Kayansalçik for sharing his experimental studies with us. I would like to thank to Asst. Prof. Dr. Altuğ Melik Başol and Doc. Dr. Ayşe Gül Güngör for their time and consideration as a referee.

The author would like to gratefully acknowledge Scientific and Technological Research Council of Turkey (TÜBİTAK) for providing financial support to this research with the 114M423 project. Also, authors thanks to to Assoc. Prof. Dr. Ismail Arı for providing computational resources to carry out preliminary numerical simulations and to Özyeğin University for providing HPC cluster. Finally, I would like to thank my dear wife Merve Yılmaz for their endless support, my dear father Ali Yılmaz for the convenience in my professional career and my mother and my motivational supporter Gül Yılmaz.

TABLE OF CONTENTS

LIST OF TABLES

LIST OF FIGURES

NOMENCLATURE

Latin Symbols

D Droplet diamater [m]

t Time [s]

t^* Non-dimensional time [-]

$\vec{g}$ Gravitational acceleration [m/s^2]

$\vec{U}$,$\vec{V}$ Velocity vector [m/s]

$\vec{U}_{cl}$ Contact line velocity [m/s]

P, p Pressure [Pa]

Ca Capillary number [-]

We Weber number [-]

We_n Normal Weber number [-]

We_t Tangential Weber number [-]

Co Courant number[-]

g_c Geometric weighting factor [-]

f Smooth factor [-]

Greek Symbols

μ Dynamic viscosity [Pa.s]

ρ Density [kg/m^3]

α Volume fraction [-]

σ Surface tension [N/m]

κ Surface Curvature [1/m]

$\vec{n}$ Surface Normal [i,j,k]

θ Contact angle [°]

θ_{adv} Advancing contact angle [°]

θ_{rec} Receding contact angle [°]

θ_{eq} Equilibrium contact angle [°]

Abbreviations

CFD Computational Fluid Dynamics

VOF Volume Of Fluid

DNS Direct Numerical Simulation

CSF Continuum Surface Force

CSS Continuum Surface Stress

SIMPLE Semi-Implicit Method For Pressure-Linked Equations

PISO Pressure-Implicit with Splitting of Operators

PIMPLE Combination of PISO And SIMPLE Algorithm

AMR Adaptive Mesh Refinement

OpenFOAM Open Field Operation and Manipulation

HF Height Funciton

FS3D Free Surface 3D

CHAPTER I

INTRODUCTION

It has many motivation sources such as the investigation of droplet surface interaction, industrial applications, meteorological phenomena, scientific observations. There are many studies in the literature regarding the interaction of drops on different physical surfaces [2],[3],[1]. Considering the study of droplets by simulations, there are many 2D and 3D simulations can be found in the literature [4],[5],[6]. By adding parameters such as surface coating characteristics, surface velocities and slope, the behavior of droplets is examined experimentally and numerically [7]. Considering the factors such as the minimum and maximum diameters of the droplets that can be created experimentally or the difficulty of surface coating techniques with different characters, the examination of the droplet surface interactions by simulations provides various advantages. Considering these advantages, many difficulties such as the establishment of droplet setup, high resolution camera shooting techniques, the shadow of the light on the drop and the measurements tolerance ; simulations are cheap and fast, the desired drop diameter, surface contact angles and liquid type can be used,easy to post-processing, the surface slope and speed limits are flexible. It is a challenging problem that droplet simulations compare with the experimental data. Difficulties of the problem include different factors such as the fact that the time scales evolve in microseconds, the tolerances are small considering the physical size, the interface provides continuity and wall interaction at the instantaneously true dynamic angle, and the surface tension works properly.

The study of droplet dynamics in a numerical environment has a significant meaning for situations where it is not possible to investigate experimentally in advanced conditions. Necessarily, numerical scenarios are in agreement with experimental data. It is a challenging problem that droplet simulations compare with the experimental data. Difficulties of the problem include different collations such as the fact that the time scales evolve in microseconds, the use of direct numerical models in a multiphase case, the tolerances are small considering the physical size, the interface provides continuity and wall interaction at the instantaneously accurate dynamic contact angle, and the surface tension works properly. It is possible to simulate stationary wall applications in 2D and avoid 3D simulation problems because axisymmetry is not broken. For moving wall simulations, an interesting question will be arised, because how do these models response in case of broken axisymmetry? Validations are compared with [1],[2],[3] test cases 3D simulations with stationary and moving wall conditions. Therefore in this paper we provide a systematic way to prepare 3D and 2D simulations which has been validated.

1.1 Literature Review

While performing drop simulations, there are 2 major problems that need to be improved

First problem is the unphysical fluid motion on the drop surface, which is mostly seen in 3D simulations and referred to as "parasitic current or spurious current" in the literature, can distort the accuracy of droplet simulations [8]. In 2D simulations, this problem can be ignored, since the droplet is examined by means of an axisymmetry condition. However, when droplets impact to moving or inclined surfaces, 3D simulations should be conducted because axisymmetry of the flow is broken. The droplet interface unphysical fluid motion disrupts the spreading and deposition form of the droplets, causing the mathematical solution and thus the deterioration of the form of the drop due to the artifical gradient it creates on the surface. "Parasitic currents are unphysical fluid motions generated when using implementations of the Continuum Surface Force technique to model surface tension forces in Eulerian-based multi-phase Computational Fluid Dynamics (CFD) calculations."[8] In the literature, unphysical flow in certain regions on the interface, which is called parasitic current or spurious current, cannot be improved with grid refinement or decreased computational time step.[8] Thus, this situation, which is grid resolution and time step independent, encouraged to study the calculation methods of κ (curvature) and $\vec{n}$ (surface normal) estimation in the CSF equation [9].AMR (Adaptive Mesh Refinement) methods [10] are used in multiphase solvers such as Gerris [11] and its new version Basilisk[12], which is an effective application to provide interface sharpness and reduce computational cost. Limitation of parasitic current with HF (Height Function) [13] method has been published in the literature. Again, with the Level-Set[14] & VOF[15] hybrid models interface representation, progress is made. In recent years , with the FS3D solver [16] developed, the primary effects of parasitic current on the interface are reduced with that hybrid Level-Set[14] & VOF[15] models [17].The use of artificial viscosity models for parasitic current suppression is used today in some VOF[15] based software [18]. It has been shown that setting the reference frame opposite motion for only small channel flow can reduce parasitic currents [19].

The second major problem is the correct calculation of contact angles, namely advancing, receding and equilibrium state, which are the parameters used to characterize the wettability of the surface, and define the instantaneous contact angles made by the droplet with the surface as the contact line of the droplet moves. The contact angle directly affects the form of spread and impact outcome.Wrong calculation of instanatenous contact angle disrupts the rate of spreading and deposition of the droplet on the surface. Therefore, contact angle models are required for the simulations to converge to the experimentally observed droplet dynamics and impact outcomes. The simulation results show that precise dynamic contact angle modelling plays critical role in modelling droplet impact [20]. Therefore, calculation models are required for the contact angle model in simulations to converge to the experimental process. Kistler contact angle model [21] appears to converge to experimental values. However, Kistler model [21] cannot accurately calculate droplet contact angles in cases contact line velocity of the drop is low or stationary (See the Sec.2.6). The development of this contact angle model appears to improve the droplet surface contact angle calculation. In this study modeled the smooth transition of the contact angle hysteresis in the transition from advancing and receding section. Considering that the contact angle has a direct effect on the dynamics of impacting droplet, the use of a contact angle model allowing a smooth transition appears compulsory to improve the droplet surface contact angle calculations [22][23]. This situation is clearly seen in FIG. 6 and FIG. 7. Considering that the contact angle has a direct effect on the spreading and deposition parameters of the droplet, it is provided with a smooth transition "modified" arrangement when we think it will make an important contribution to drop simulations in open-source OpenFoam CFD toolbox.

Inertia dominates over viscous flow cases are performed in theoretical and numerical comparison studies [24]. Viscous boundary layer and splashing dynamics were examined in thin film studies. It has been shown that film thickness and surrounding gas also plays critical role in splash formation [25] [26]. [6] Simulations with CLSVOF hybrid methods were also performed for thin film studies [27]. For hemispherical droplet forms, which we frequently encounter in experimental studies, the impact process and drop physics were studied [28].

In spite of the developments towards correct estimation of κ (curvature) and $\vec{n}$ (surface normal) estimation with height function approximations or hybrid Level-Set&VOF models [13] [16] [17], there remains always a certain amount of discretization error. Moreover, both curvature and surface normal depends on the gradient approximation of liquid fraction at the droplet surface in the CSF model. We predict that the accumulation of gradient calculation errors at certain directions (angles) of droplet propagation, dictated by the type computational cell, as the main source of the problem. Appearance of this situation, which is grid resolution and time step independent, encouraged us to study dependence of the gradient calculation in the CSF formulation to the used computational cell.

In this study, the droplet dynamics is investigated with the Interfoam solver of 3-D OpenFoam software which is developed for multiphase flows. This solver uses the VOF method, it solves the transport equation for the volume fraction of the liquid phase. However, the standart multiphase solver (interFoam) uses its own static or dynamic value calculations for contact angle. In this study, a new solver was created by using Kistler dynamic contact angle libraries developed by Berberovic [29]. Furthermore, the contact angle model has been modified to have a smoother transition between advancing and receeding phases of droplet motion on the surface.

1.2 Objective

The aim of this study is to simulate the behavior of droplet impacting stationary and moving hydrophobic smooth surfaces. Impact outcome and spreading measurements were analyzed according to the surface velocities of the droplets on the regime map.

1.3 Hypothesis

In this study, it was investigated that a VOF based multiphase simulation with an accurate response of the contact angle model for all dynamic velocities of the droplet and limiting the parasitic current effects will produce results comparable to the experimental data and reduce the load of the experimental investigation.

1.4 Methodology

In this study, the droplet dynamics was investigated in 3-D "OpenFoam" software in "interFoam" solver developed for multiphase flows."The solver solves the Navier Stokes equations for two incompressible, isothermal immiscible fluids. That means that the material properties are constant in the region filled by one of the two fluid except at the interphase." This solver uses the VOF method, it solves the transport equations for field functions with two phases volume fraction. In multiphase flow problems (liquid-gas); the phases are separated by a moving and deformed interface. This dynamic interface should evolve by considering the surface tension effect. And also the correct calculation of the surface tension is possible only with the continuity of the surface curvature. Finally, the interface will make the wall contact at an accurate angle, allowing the surface to evolve correctly. The interFoam multiphase solver uses its classical static or dynamic calculations for contact angle. The simulations using these models didn't provide physical results. The droplet spreading&splashing rates were not captured by dynamic and static contact angle implementations. The deviations in this ratio have shown us that the contact angle has a critical role in calculating the surface tension forces. For this reason, multiphase solver should be modified with Kistler model [21] contact angle implementations for dynamic contact angle model. A new solver myinterFoam was created by using Kistler dynamic contact angle libraries developed by Berberovic.[29]

CHAPTER II

SIMULATION

2.1 Numerical Method

In this study, VOF method was used for multiphase flow simulations. The continuity, momentum equations and the transport equation for the volume fraction of liquid phase are simultaneously solved. The flow is assumed to be incompressible, immiscible and newtonian. All conservation equations can be written in terms of a general transport equation by integral form :

$$\underbrace{\frac{d}{dt}\int_V \rho\phi \; dV}_{\text{Transient Term}} + \underbrace{\int_A \rho v\phi . \; da}_{\text{Convective Flux}} = \underbrace{\int_A \Gamma\nabla\phi \; da}_{\text{Diffusive Flux}} + \underbrace{\int_V S_\phi \; dV}_{\text{Source Term}} \tag{1}$$

where ϕ can be any scalar. It is 1 for the continuity equation and it is equal to any component of velocity vector for the momentum eqution. V is the control volume and a is surface area of the control volume. Γ is diffusion coefficent in diffusive flux term and in the present problem only the diffusion of momentum is considered, i.e it becomes the dynamic viscosity in the momentum equation.

Dynamic viscosity and mixture density equations can be written as function of volume fractions α forms below:

$$\rho = \alpha\rho l + (1-\alpha)\rho g \tag{2}$$

$$\mu = \alpha\mu l + (1-\alpha)\mu g \tag{3}$$

$$\frac{\partial\alpha}{\partial t} + \nabla.(\alpha\vec{U}) - \nabla.(\alpha(1-\alpha)U_r) = 0 \tag{4}$$

where $(\nabla.(\alpha(1-\alpha)U_r))$ is the artificial compression term [30]

Artificial compression U_r is a normal velocity field. This velocity field applies artificial compression on the surface. Artificial compression velocity is setting by C_α (*cAlpha*) in OpenFoam (See Eq. 5) . The zero value for cAlpha applies no compression and higher values introduce the artificial velocities at the interface [31]. Artificial compression term ensures the stability of interface diffusion (see section 2.7 for further discussion).$\vec{U}$ is the velocity of fluid, p is pressure, g is gravitational force ,F_s is surface tension force represented by volume.

$$U_r = C_\alpha \times |v| \frac{\nabla\alpha}{|\nabla\alpha|} \tag{5}$$

Surface tension force (F_s) in CSF model, which is one of the source terms in the momentum equation formulated by Eq. 1. needs the calculation of (surface normal) $\vec{n}$ and (surface curvature) κ

$$F_s = \sigma\kappa\vec{n} \tag{6}$$

$$\vec{n} = (\nabla\alpha) \tag{7}$$

$$\kappa = \nabla.(\frac{\nabla\alpha}{|\nabla\alpha|}) \tag{8}$$

2.2 3D Model

As can be seen in FIG.1 below, in this example the drop is located in the axisimetric center of the domain close to the impact surface. The liquid phase in the simulation represents the α= 1 value in red and the air phase represents the α= 0 value in blue.

The reason for creating 6 different domains above is due to parameters such as drop diameter, spreading velocity and spreading&deposition size in simulations.

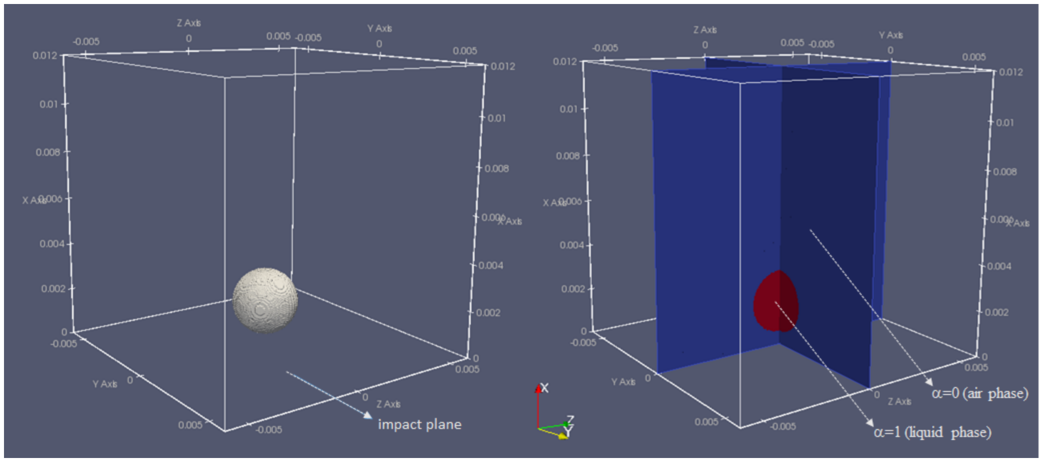

Figure 1: Conceptual computational domain and volume fraction with initial conditions, partial rebound case are shown as examples.

2.3 Unphysical Flows

"Parasitic currents are unphysical fluid motions generated when using implementations of the Continuum Surface Force technique to model surface tension forces in Eulerian-based multi-phase Computational Fluid Dynamics calculations."[8].In this study it was found that there was a correlation between parasitic current and unit volume and mesh distribution on spreading plane. The source of this correlation comes from gradient calculations that directly effect parasitic current. The same two drop simulations of physical conditions examined with Cartesian and Polyhedral mesh type showed different gradient distribution on the interface in the motion where surface tension forces started to dominate. Simulations that can observe the behavior of droplets, especially in the propagation plane, which are a flow dominated by surface tension forces, were examined and gradient shifts in the diagonal axis of the spreading axis were calculated and shown. The results here also support our mesh type hypothesis in spreading plane, it was mentioned that Continuum Surface Force CSF (See Eq. (6)) equivalence is used to calculate surface tension forces.In this equation, surface normal ($\vec{n}$) (See Eq. (7)) and curvature (κ) (See Eq. (8)) values are used to calculate the gradient of the alpha term.

CSF Eq. (6)

$$F_s = \sigma\kappa\vec{n}$$

Surface normal Eq. (7)

$$\vec{n} = (\nabla\alpha)$$

Curvature Eq. (8)

$$\kappa = \nabla.(\frac{\nabla\alpha}{|\nabla\alpha|})$$

Incorrect gradient values calculated in the propagation plane disrupt the surface tension- inertia balance and create unphysical currents. Especially, the simulations having polyhedral mesh structure in the spread plane have well distributed scalar and vectorel field values on the interface.

2.4 Gradient Calculations

It was mentioned that Continuum Surface Force CSF (See Eq. 6) equivalence is used to calculate surface tension forces. In this equation, surface normal ($\vec{n}$) (See Eq. 7) and curvature (κ) (See Eq. (8)) values are used to calculate the gradient of the volume fraction (α). In Fig. 2, the gradient of the volume fraction for normal impact simulations on wax surface simulation with 1mm droplet diameter and 25.48 normal Weber number value is shown for cartesian and polyhedral mesh types in the spreading plane. In those simulation, there is no interface compression and the grid resolution is comparable. Parasitic current, which is encountered with unphysical interface problems in drop simulations, gives different results in cartesian and polyhedral mesh structure. It can be seen that volume fraction (α) gradient values are has better distribution for the polyhedral grid and the error has an accumulating nature in certain directions. Incorrect gradient values calculated in the propagation

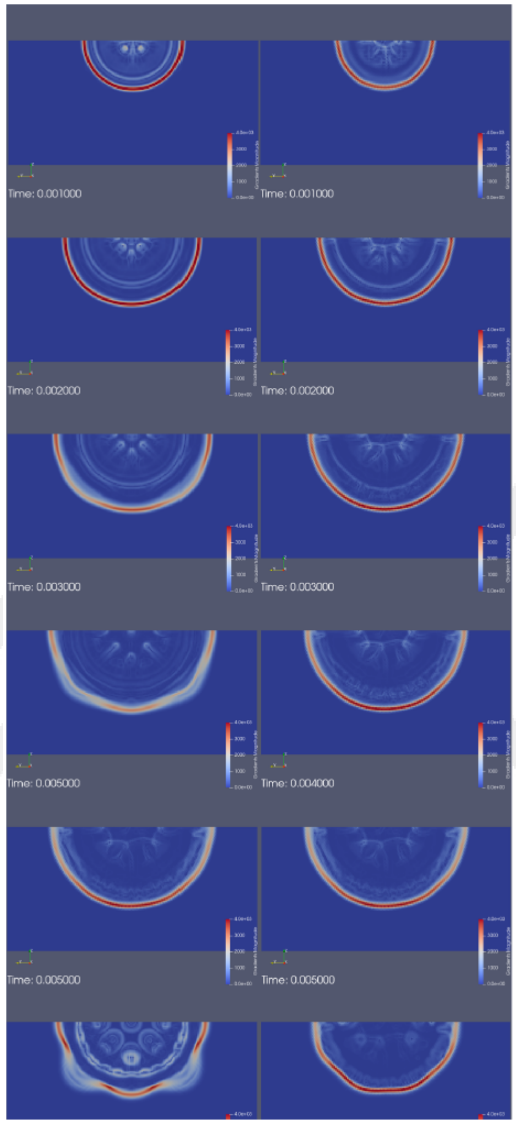

(a) (b)

Figure 2: Time evolution of alpha gradient value at the interface. (a) Cartesian grid based simulational domain. (b) Polyhedral grid based simulational domain.

plane disrupt the surface tension-inertia balance and create unphysical currents. Especially, the simulations having polyhedral mesh structure in the spread plane have well distributed scalar and vectorel field values on the interface. It is fair to argue that polyhedral grid distribution should give more accurate evolution of drop shape compared to cartesian grid distribution. These results support our hypothesis, that mesh type in the spreading plane has an effect on the accumulating effect of Parasitic

Current.

How the shape of computational cell influence the gradient calculation and the prefered direction of error accumulation and the dependency of error on gird reolution can be best studied by a simple toy-problem. For this purpose, in 2D and static conditions, the gradient of volume fraction at the interface of a circular droplet is numerically analyzed with cartesian and polyhedral (hexagonal) mesh types. Cell-centered Gauss-Green method is used in gradient calculations. Gradient at the centroid of an element C with volume V is computed as:

$$\nabla \phi_C = \frac{1}{V_C} \sum_{f \sim nb(C)} \phi_f S_f \tag{9}$$

where S refers to surface vector and f refers to a face. And also ϕ is defined with avarage values according the distance ratio of the two cell sharing the face .

$$\phi_f = g_C \phi_C + (1 - g_C)\phi_F \tag{10}$$

where g_c is a geometric weighting factor.

It can be seen in the FIG. 3 that the gradient values calculated by mathematical modeling are affected by the type of mesh in the spreading plane. Each center has 4 neighbors and edges in the cartesian grid and 6 neighbors and edges in the polyhedral (hexagonal) grid. Hence, according to the graident calculation formulation, polyhedral grid utilizes information from higher number of neighbouring cells. The magnitude of gradient vector clearly shows elevated values every 90 degree in FIG. 3.

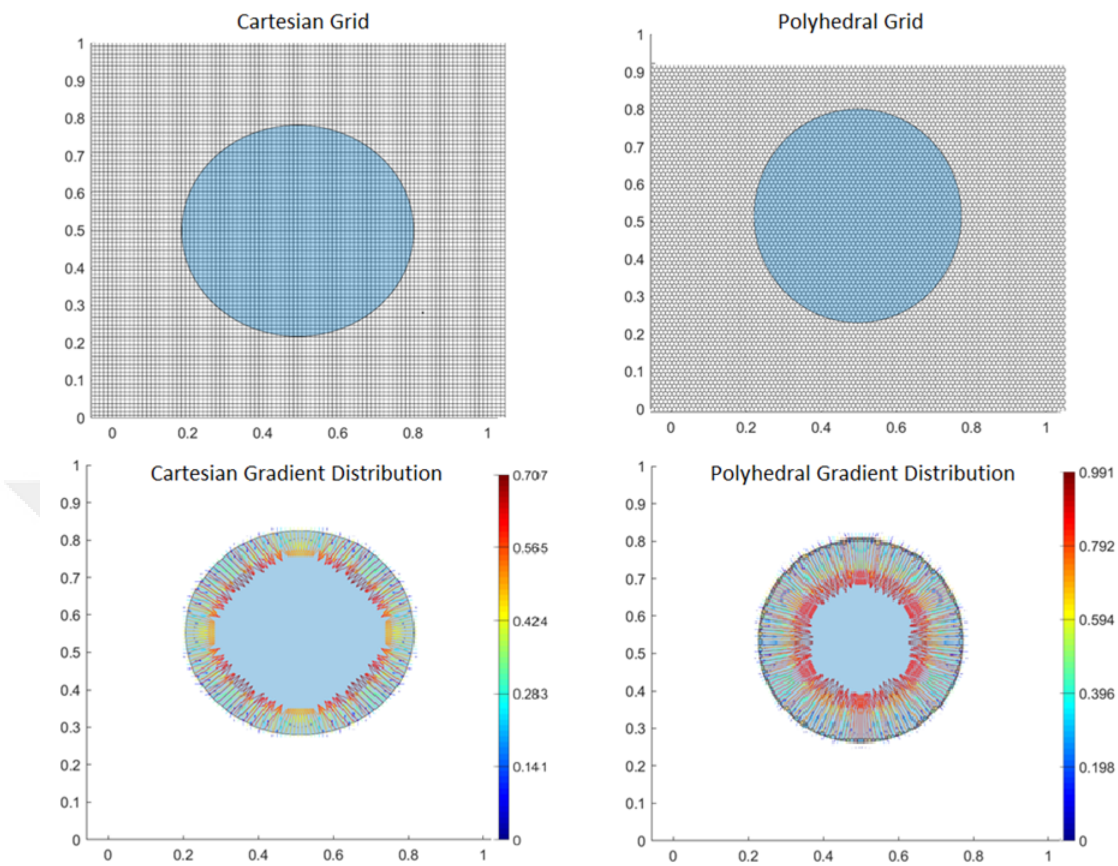

Figure 3: 2D represantation of gradient calculation on interface . (a) Cell centered gradients are calculated by cartesian cell and 4 neigbor. (b) Cell centered gradients are calculated by polyhedral cell and 6 neigbor.

When the distribution of gradient values normalized by the maximum magnitude is analysed as a function of polar angle θ (FIG. 4a), it is seen on the left side of the figure that there is a difference of up to 25% between the largest and smallest gradient values calculated on the interface for the cartesian grid. When the distribution of gradient values calculated by polyhedral gradient distribution is examined (FIG. 4b) , it is observed that the difference between the largest and smallest gradient values calculated on the interface falls to an average of 8-12%. When the gradient distribution is examined, it is observed that the gradient values peak at every 90 degrees on the 360-degree interface for cartesian grid distribution, and in polyhedral grid, these values are repeated on average at every 60 degrees and with relatively low amplitudes.

In the same figure, the grid resolution is also varied and, surprisingly no reduction in the amplitude of oscillations is observed. This simple analysis clearly shows that the grid type and the number of neighboring cells used in gradient calculations are more important than the mesh resolution when calculating the gradient. Moreover, the direction of error accumulation is dependent on the number of the neighboring cells. In other words, in gradient calculations, the polyhedral grid structure would provide smoother distribution of volume fraction gradient compared to the cartesian grid structure.

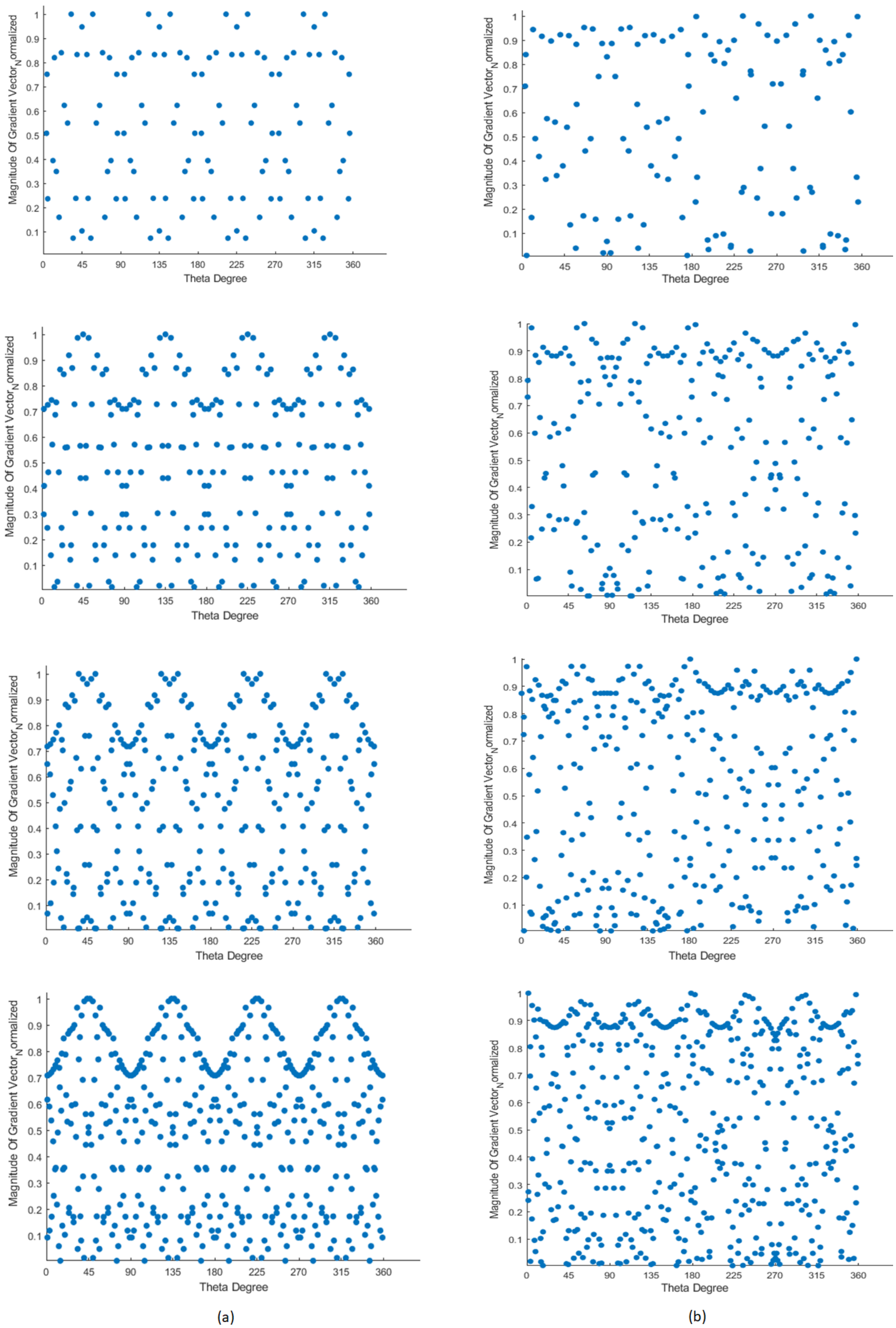

Figure 4: The 4 comparable analyzes that normalized magnitude of gradient value ordered from top to bottom were calculated with 24x24, 48x48, 64x64, 96x96 grid resolutions. (a) Cartesian grid results. (b) Polyhedral grid results.

It should be noted that AMR (Adaptive Mesh Refinement) applications have gained importance in order to reduce computational costs, and AMR applications preffers the cartesian form of the grid [12]. Although AMR applications reduce computational cost especially in 3D simulations, no matter how fine the grid resolution is, it will not contribute to the elimination of interfacial unphysical flows.

2.5 Mesh Generation

In the present study the domain and spreading plane are meshed with polyhedral grid to have smoother calcualtions of volume fraction gradient and reduce the accumulating effect of parasitic current as explained in the previous section. Star-ccm+'s mesh generator was used to generate polyhedral mesh with volumetric control. An example of the computational mesh is shown in Fig. 5.The created mesh was converted to OpenFoam mesh with $ccm26foam$ utility. The Tables 1 , 3 and 5 . test cases and number of grids for 10 different droplet simulations are given. 6 different domains are created due to the variations in parameters such as drop diameter, spreading velocity and spreading & splashing size in the simulations. In order to increase the accuracy, it is necessary to increase the grid resolution, but increasing the number of grid cells beyond certain limits increases computational time exponentially because of the limits set to the mean and interface Courant number to ensure stability.

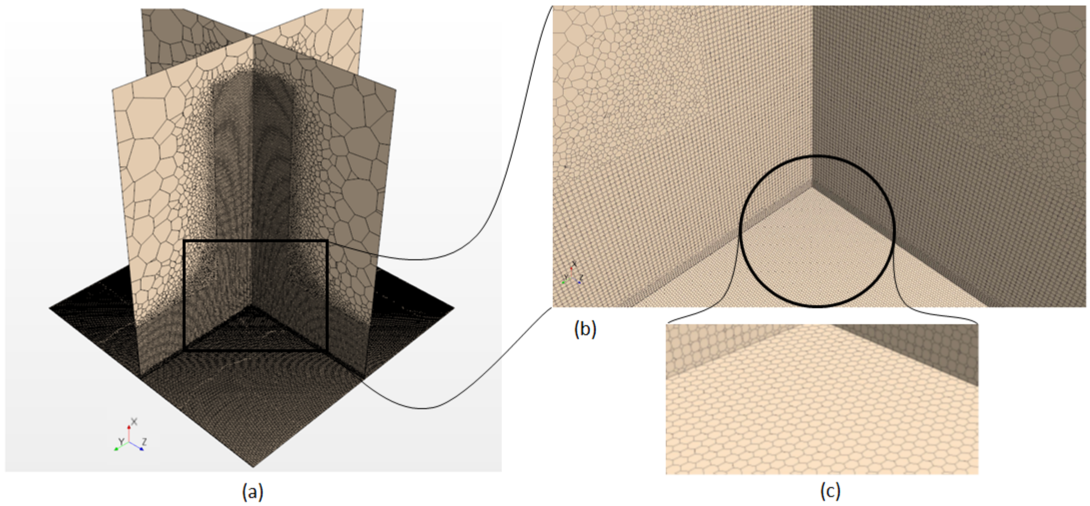

Figure 5: Full Geometric Mesh and Plane Mesh Distribution

Table 1: The size of 6 created domain with respect to wall velocity and maximum spreading diameter.

Case	Outcome	Experiment	Wall Cond.	Domain (mm)	Cell no.
1	Partial Rebound	Rioboo et al., 2002	Stationary	12x12x12	5,639,031
2	Deposition	Kayansalcik, 2018	Stationary	3x4.4x4.4	6,177,494
3	Partial Rebound	Kayansalcik, 2018	Stationary	3x4.4x4.4	6,177,494
4	Deposition	Kayansalcik, 2018	Moving	1.6x2.8x5.5	3,723,654
5	Deposition	Kayansalcik, 2018	Moving	1.6x2.8x5.5	3,723,654
6	Deposition	Kayansalcik, 2018	Moving	1.6x2.8x5.5	3,723,654
7	Deposition	Kayansalcik, 2018	Moving	1.5x2x9	2,652,502
8	Deposition	Chen & Wang, 2005	Moving	1.5x2x12	2,651,688
9	Partial Rebound	Chen & Wang, 2005	Moving	1.5x2x12	2,651,688
10	Split Deposition	Chen & Wang, 2005	Moving	0.8x2x9	5,361,190

2.6 Dynamic Contact Angle Model Implementation

Kistler[21] model is a dynamic contact angle model, which is not implemented in OpenFoam, Gerris, Basilisk standard solver. The OpenFoam "dynamicKistlerAlpha-ContactAngle" of [29] is modified to smooth the transition between advancing and receeding phases of droplet motion. With this new boundary field new OpenFoam multiphase solver is formed.

Standard Kistler model takes instant contact line velocity data, calculates the Capillary number dynamicaly, then calculates a new contact angle with the help of the

Hoffman [32] function and inverse of Hoffman function. That function is formulated as below;

$$\theta_k = f_{hoff}[Ca + f^{-}1_{hoff}(\theta_s)] \tag{11}$$

$$f_{hoff}(x) = acos[1 - 2tanh(5.16(\frac{x}{1 + 1.31x^{0.99}})^{0.706})] \tag{12}$$

and the Capillary number is defined as;

$$Ca = \frac{\mu * U_{cl}}{\sigma} \tag{13}$$

θ_s is either advancing or receding contact angle depending the direction of the contact line motion, θ_k is Kistler dynamic contact angle, θ_e is equilibrium contact angle , θ_d is modified kistler dynamic contact angle, μ is dynamic viscosity, U_{cl} is the instantaneous velocity of the contact line and σ is surface tension coefficent.

As can be seen in the FIG. 6, capillary number was found to be below certain values during simulation. Especially in stationary surface applications, the contact angle is some times close to equilibrium state. At the rest of motion of those advancing and receding phases, hysterisis state should be smooth transition in close statement as the case of "pinning" in the literature [33] and in the standing surface models. For example the rioboo case, the standard Kistler model has advancing phase with an angle of $\theta_{Adv} = 105$ and receding phase with angle of $\theta_{Rec} = 95$. It switches from spreading to splashing with a difference of 10 degrees. Especially for cases where Advancing and Receding contact angle difference is more than that value (ex:paraffin and teflon surfaces), the sudden transition causes the droplet affecting the spreading and deposition behaviour.

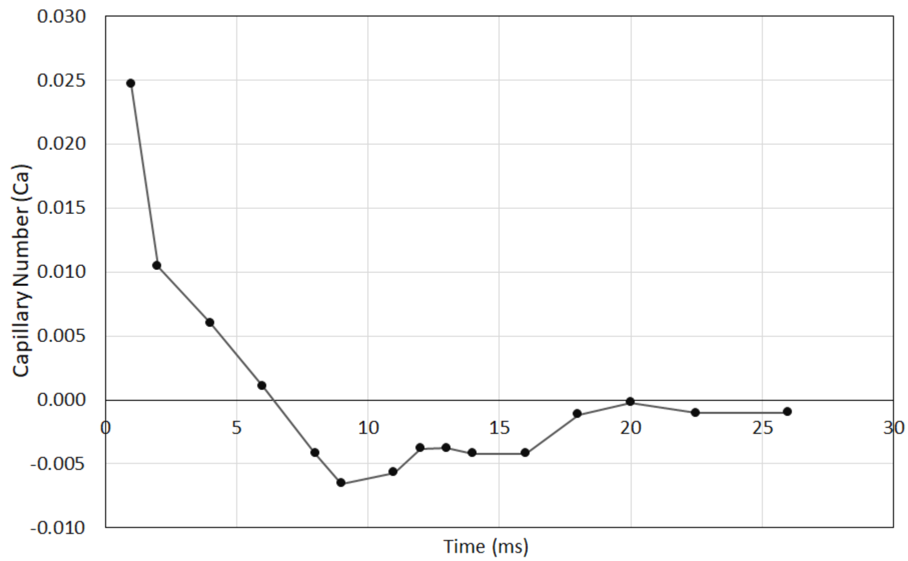

Figure 6: Instantanous Capillary number (Ca) during the Rioboo [1] simulation, respect to contact line velocity

Smooth transition has been achieved by implementing the 2 equations Eq.14 and Eq.15 shown below into the standard Kistler dynamic contact angle model.

Smoothing factor [34] equation determines the how fast transiton is occur;

$$f = 0.5 + 0.5cos(\frac{Ca}{Ca_{eq}}\pi) \tag{14}$$

Modified dynamic kistler contact angle equation;

$$\theta_d = f\theta_e + (1-f)\theta_k \tag{15}$$

As can be seen from the FIG. 7 , the standard kistler model creates hysteresis with a low capillary number during the transition zone , depending on the difference between advancing and receding contact angles. This situation cannot respond to pinning state simulations. The modified kistler contact angle model provides smooth transition for pinning state. The important input here is which under capillary number state the transition curve should start for.Since the smoother function capillary number provides transitions at values 0.002 and below, Ca$_{eq}$: 0.002 value is chosen in the example.

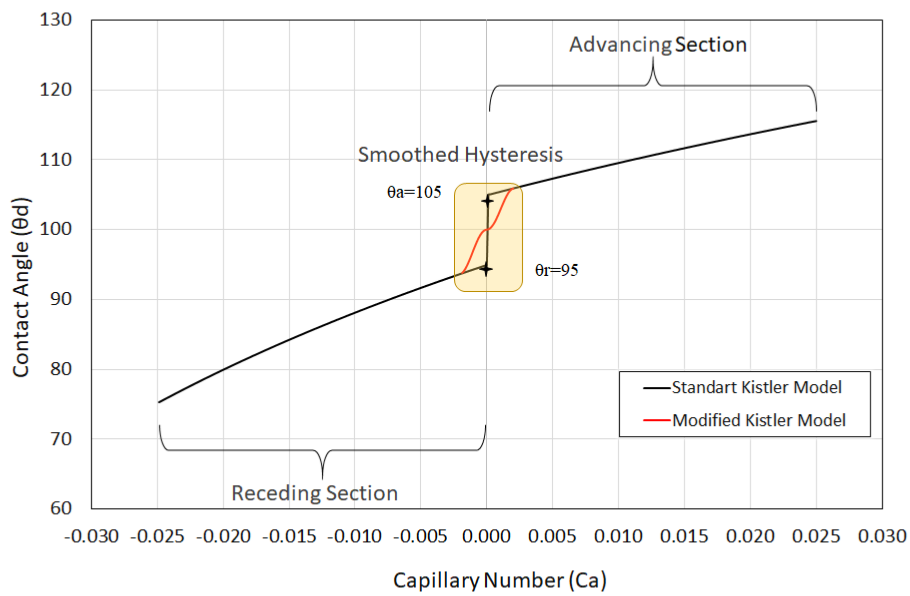

Figure 7: Modified and standart Kistler model behaviour respect to Capillary number

2.7 Numerical Schemes

Time deriatives are defined with second order implicit, bounded and modified Crank-Nicolson [35] method with the coefficent of off-centering fixed at 0.8. For this coefficent,1 refers to pure Crank-Nicolson method, 0 refers to Euler method. Numerical results converges with an adjustable time step in the range of 1e-07 s and 1e-08 s.

Gradients are calculated with different schemes. Velocity gradient terms is defined with Gauss Linear method. Linear interpolation schemes is working with central differencing method. But α gradient terms is discretized by gauss cubic interpolation scheme. Cubic interpolation provides stability to gradient calculations in low diffusion situations. Gaussian integration is default finite volume concept, which requires the interpolation of values from cell centres to face centres. As can be seen in FIG.8, stabilization of diffusion is achieved by cubic interpolation and the interface compression term is 0.24 $cAlpha$ value. As can be seen in (Eq. 4), interface compression velocity is included in term alpha transport equation gradient calculations. The approach of this value to 0 increases the interface diffusion, approaching 1 decreases the diffusion, but at the same time causes physical fluctuations and parasitic forces to occur at the interface. Interface compression term provides stability in simulations at different values depending on the kinematic conditions of the droplet. For the simulations conducted here, all *cAlpha* value was given in Table. 3 in stationary wall section and Table. 5 in moving wall section .

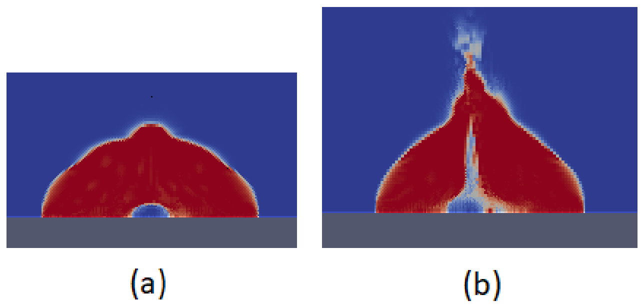

Figure 8: Comparison of diffusion reduction by interface compression and alpha gradient methods.(Case 1)
(a) cAlpha: 0.24 was calculated by alpha gradient cubic interpolation, (b) cAlpha: 0.1, alpha gradient linear interpolation. Red represents water, blue represents air on Figure.

Divergence schemes are used to discretize to convective terms. In the present simulation settings, Linear-upwind (second order, upwind-biased, unbounded, that requires discretisation of the velocity gradient to be specified) methods is used for the velocity terms. For the liquid fraction, Gauss Linear, which is widely used in multiphase solvers. It was observed that, gauss linear-upwind interpolation schemes reduced the computational time compared to gauss linear method. Closer examination of the simulations revealed that the gauss linear method created oscillation and therefore the number of iterations increased to meet the convergence criterion at each time step. Therefore, the Gaussian linear-upwind method has been selected to provide more stable results for such solutions.

By looking the figure upward, the face values appearing in the convective flux can

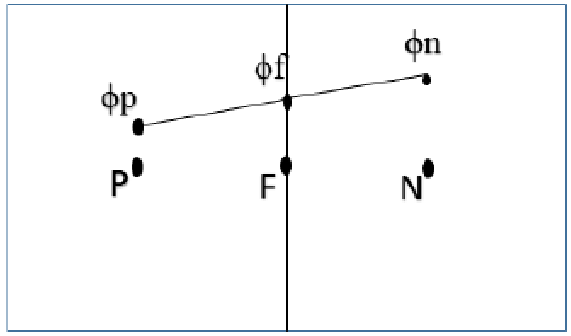

Figure 9: Linear Interpolation

By looking the figure upward, the face values appearing in the convective flux can be computed as follows;

$$\phi f = f_x P + (1 - f_x)\phi N$$

$$f_x = \frac{fN}{PN} = \frac{x_f - x_N}{d}$$

Gauss linear method is second order acuurate but it may generate oscillatory solution with unbounded solution.

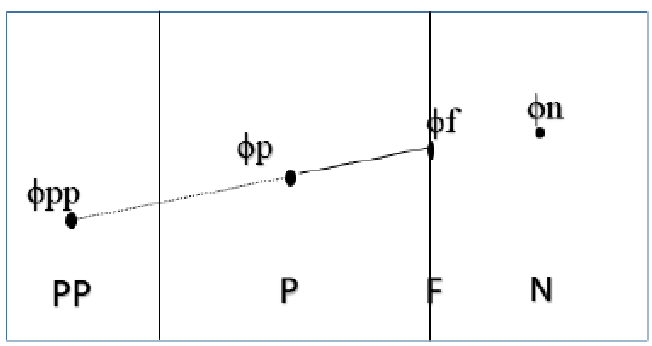

Figure 10: Linear-Upwind Interpolation

be computed as follows;

$$\phi f = \phi P + \frac{1}{2}(\phi P - \phi PP)$$

Gauss linear-upwind methods is also second order accurate but it generate more stable solutions. This method used gradient of $\nabla\phi$ to improve accuracy of extrapolation. This method gives coherent behaviour for convective terms.

Laplacian Scheme:For this scheme, Gauss Linear Corrected method is used. This scheme contains Laplacian terms (ex:diffusion term in momentum eq.) That method also use linear interpolation (second order).

It was observed that, gauss linear-upwind interpolation schemes reduced to computational time compared to gauss linear method. When we examined the methods, it was concluded that the gauss linear method created oscillation and therefore the number of iterations increased and the simulation time extended to meet the convergence criterion. The Gaussian linear-upwind method has been shown to provide more stable results for such solutions.

Solution tolerance was defined 1e-8 under "fvsolution" dictionary for all field functions (Velocity,Pressure,Alpha(volume fraction)). The iteration algorithm on this case, PIMPLE was used. That method is combination of PISO and SIMPLE ([36]) ([37]) algorithm. Generally that method is created to use for transient case as most of multiphase simulations.In that algorithm, some parameters should be defined by user. For ex:nCorrector is defined to 4 in this case, that means ; sets the number of times the algorithm solvers the pressure eq. and momentum corrector in each step. In that methods many inner and outher iteration can be defined as alphasubcycles, ortogonal corrector, alpha corrector etc..

The case structure solved with OpenFoam interFoam solver is shown in the figure below.

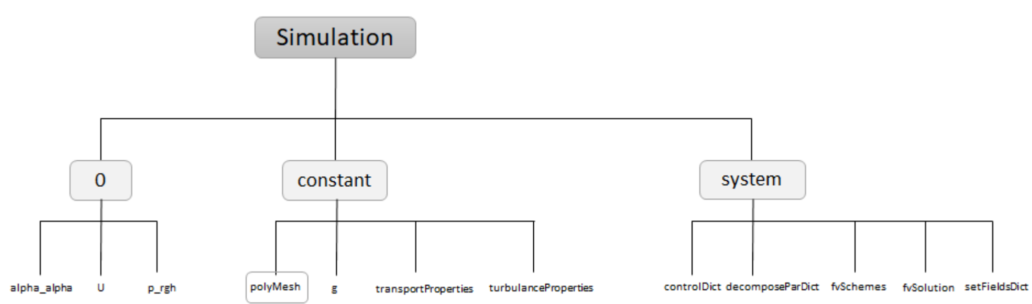

Figure 11: Case structure of interFoam

There are 3 folders in the main simulation folder. The 0 folder includes the boundary velocity conditions, pressure, alpha phase fraction. The constant folder includes the mesh directories, gravity condition, turbulance properties and fluid properties . The system subdirectory includes time control, solver method control, discretization schemes and initial phase conditions.

2.8 HPC Cluster

The HPC cluster is located in Özyeğin University engineering faculty. We had to continue our simulations with HPC cluster instead of workstation due to increased computational time. The Cluster can run simulations with 10 parallel and additional 2 serial nodes, with a total of 12 nodes and 336 processors. Our simulations give results in an average of 3-4 weeks with HPC, 2 nodes, 56 parallel processors and 1-e8 s adjustable time step according with acceptable courant number criterias. "mpirun" library is used in slurm operating system for parallel computation.

CHAPTER III

DROPLET IMPACTS ON SMOOTH STATIONARY WALL

In this section, experimental results and simulation results were compared in specific time sequences. Stationary smooth surface simulations, different surface coating materials and their responses at the contact angles specified in the results are shown with physical image and non-dimensional spread factor. The ratio of the droplet inertia-surface tension relationship is characterized by non-dimentional We_n and We_t numbers for normal and tangential forces. In droplet experiments, attention has been paid to select the following simulation data in different regime map regions with We_n and We_t values. Comparative results for 2 different outcomes are shown with 3 selected simulations. Experimental data are generally compared with the 3D simulation results, and the simulations with the opportunity to compare the experimental data are compared with the spread factor chart and the instantaneous spread diameter values of the drop. As can be seen from the comparable figure, spreading and splashing processes are developed in accordance with the experiment. To better understand these processes, spread factor chart will help.

3 different test results were simulated under the conditions of the statinary wall ($We_t = 0$). Surface material, We_n and We_t values, Advancing , Receding, Equlibrium contact angle values are given in the Table 3. The results of the experiment with FIG.12 were compared with the 2D and 3D simulation results.FIG. 14 and FIG. 16 experimental results were compared with the 3D simulation results. The spread factor charts for these 3 simulations are shown in FIG. 13, FIG. 15 and FIG. 17, respectively. According to the results of these 3 cases, the spread factor data, which

we have the opportunity to compare the spreading and deposition diameters of the drop, and the results of the experiment and simulation converge. In addition to these, when the instantaneus figure of the drop is compared, the results of the static surface experiments and simulations converge.

Table 2: Number of grid cells and droplet diameter for stationary wall cases.

Outcome	Experiment	Domain Size (mm)	No. of grid cells
Partial Rebound	Rioboo [1]	12x12x12	5,639,031
Deposition	Kayansalcik [2]	3x4.4x4.4	6,177,494
Partial Rebound	Kayansalcik [2]	3x4.4x4.4	6,177,494

Table 3: Impact conditions for the all stationary wall validation cases

Case	Surf. Material	We_n	We_t	Drop. Size	θ_{adv}	θ_{rec}	θ_{eq}	$cAlpha$
1	Wax	52	0	2.75 (mm)	105°	95°	100°	0.26
2	Paraffin	35.88	0	1.27 (mm)	113°	63°	104°	0.25
3	Paraffin	93.53	0	0.88 (mm)	113°	63°	104°	0.25

3.1 Results and Discussion

Radial spread factors data are given in all experimental cases, which we have the opportunity to compare the spreading and deposition diameters of the drop on radial direction. Radial spread factor is defined with the ratio of initial drop diameter and instant spread diameter of drop. Non-dimensional time is defined as:

$$t^* = \frac{v.t}{D} \tag{1}$$

where t is time, v is initial velocity, D is initial drop diameter.

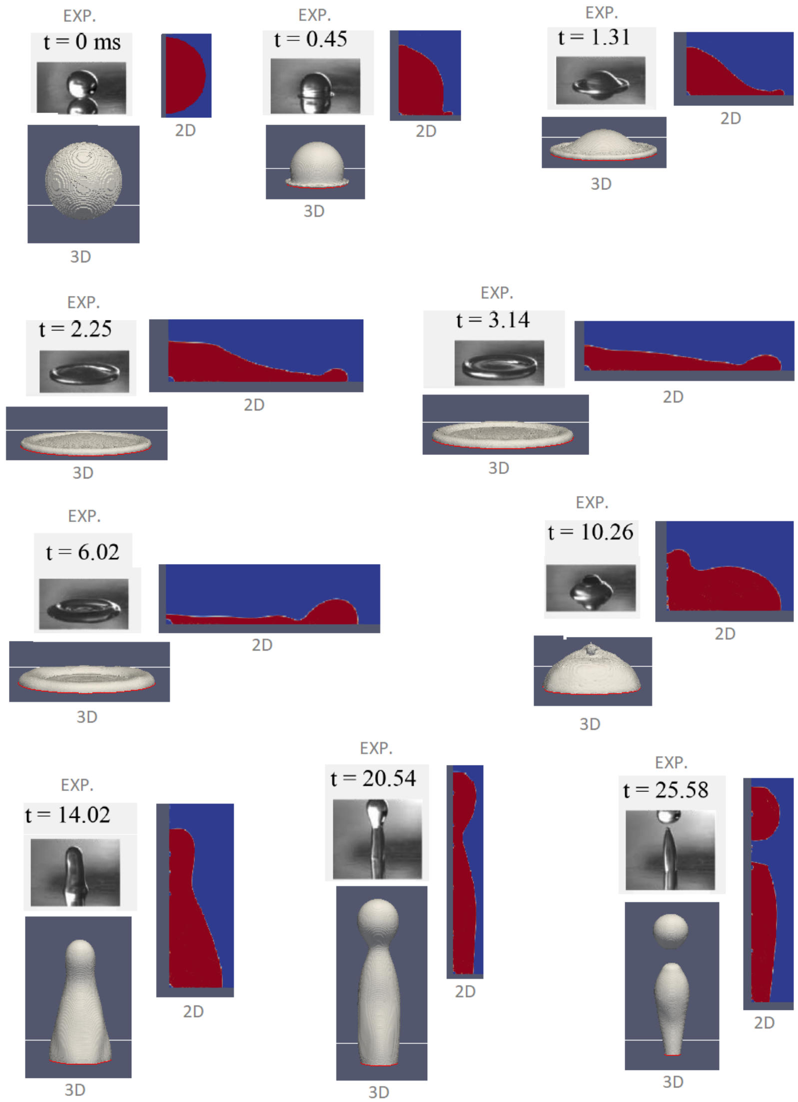

Figure 12: Time evolution of water drop impact on stationary wax surface with partial rebound outcome. Simulated images are extracted from 3D and 2D simulation results (Case 1). Time slots are shown in milliseconds. Experimental images are taken from Experiments in Fluids, Time evolution of liquid drop impact onto solid, dry surfaces, 33, 2002, pp 112-124, R. Rioboo, M. Marengo and C. Tropea, with permission will taken of Springer.

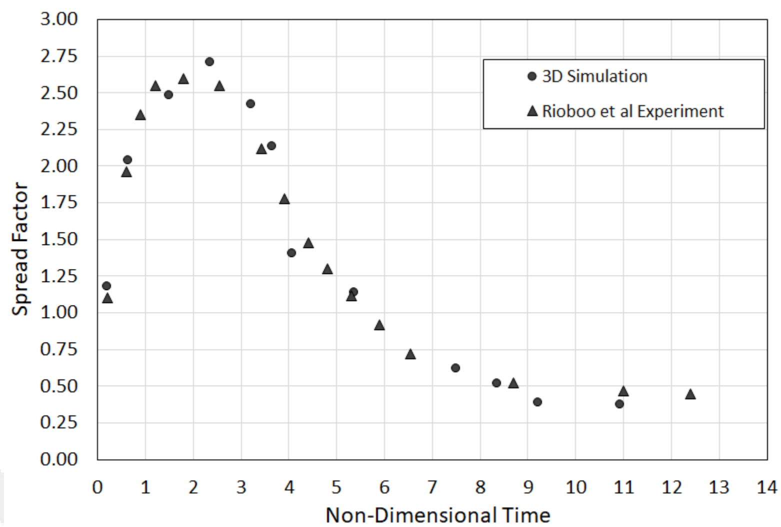

Figure 13: Non-dimensional spread factor versus non-dimensional time showing the evolution of the spread factor for reference partial rebound case (Case 1).

In Case 1, the droplet impact on the stationary wax surface was simulated both 2D and 3D domain. At the end of the experiment of droplet motion, it gives a partial rebound outcome. As can be seen from the Fig. 12, a partial rebound outcome was achieved. As can be seen from Fig. 13, the droplet nondimensional spread factor was converged .

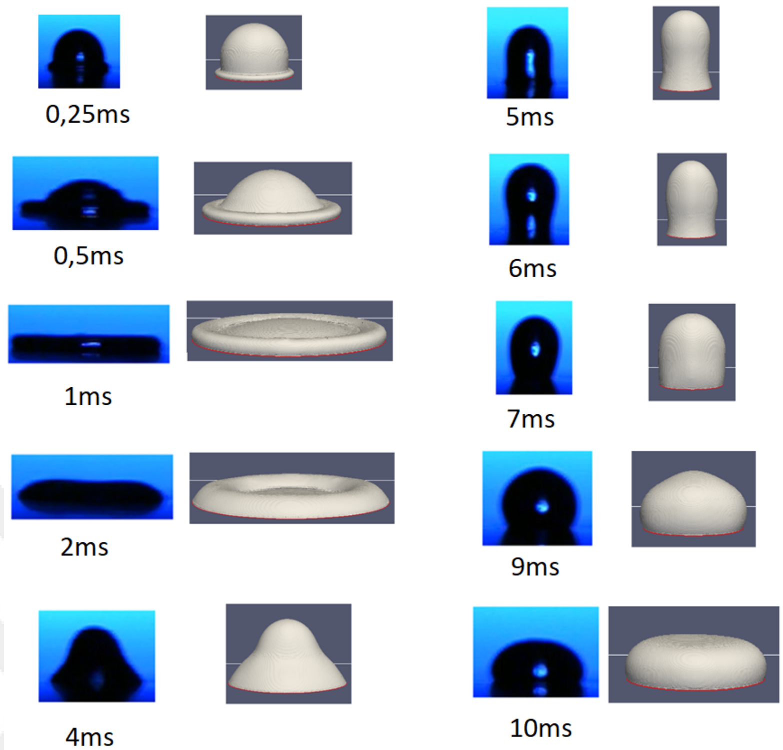

Figure 14: Time evolution of water drop impact on stationary wax surface with deposition outcome. Simulated images are extracted from 3D simulation results (Case 2). Time slots are shown in milliseconds. Experimental images are taken from Kayansalcik [2].

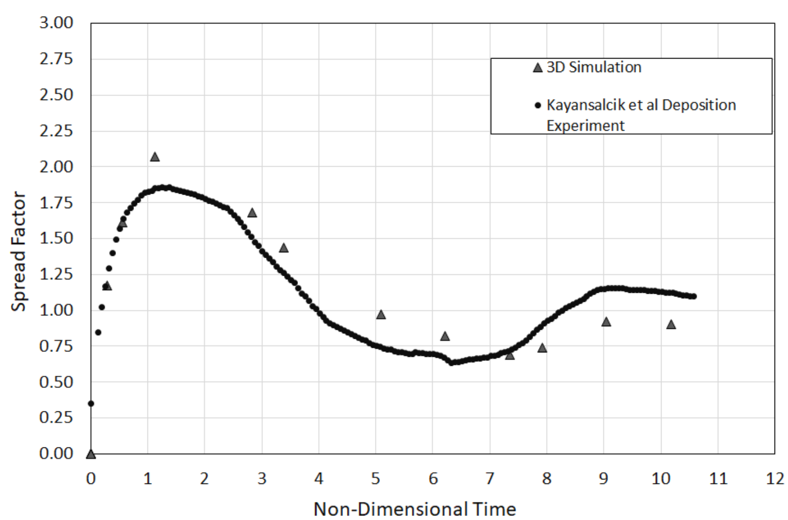

Figure 15: Non-dimensional spread factor versus non-dimensional time showing the evolution of the spread factor for reference deposition case (Case 2).

In Case 2, the droplet impact on the stationary paraffin surface was simulated in 3D. At the end of the experiment of droplet motion, it gives a deposition outcome. As can be seen from the Fig. 14, a deposition outcome was achieved. As can be seen from Fig. 15, the droplet nondimensional spread factor was converged .

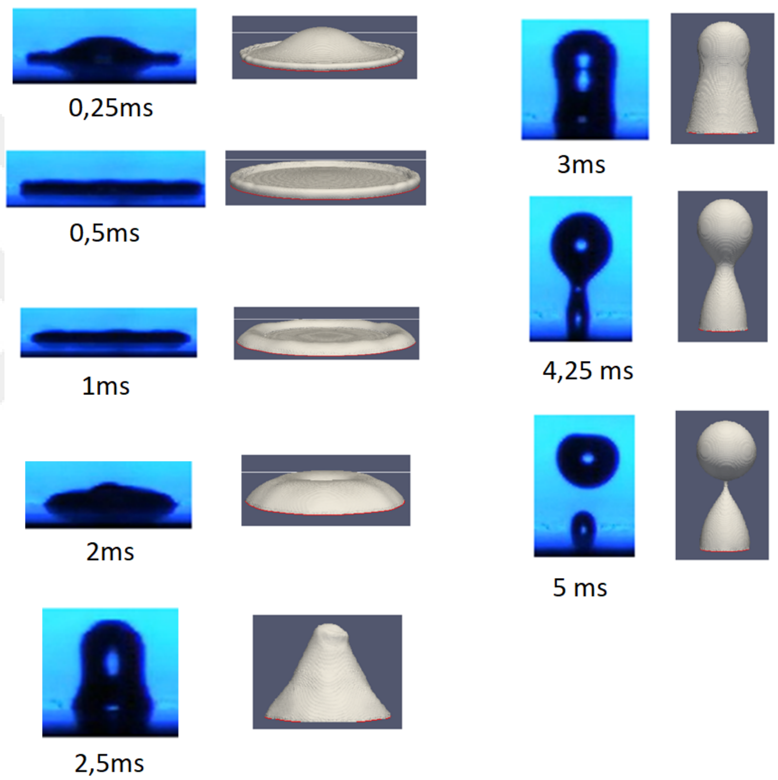

Figure 16: Time evolution of water drop impact on stationary wax surface with partial rebound outcome. Simulated images are extracted from 3D simulation results (Case 3). Time slots are shown in milliseconds. Experimental images are taken from Kayansalcik [2].

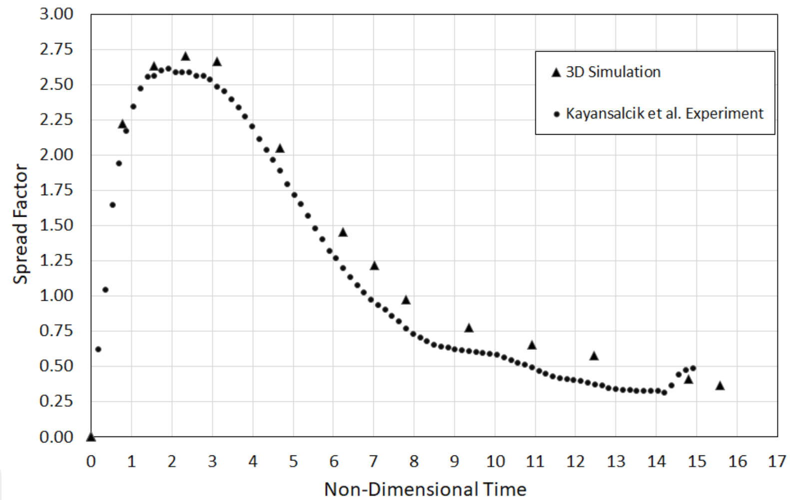

Figure 17: Non-dimensional spread factor versus non-dimensional time showing the evolution of the spread factor for reference partial rebound case (Case 3).

In Case 3, the droplet impact on the stationary paraffin surface was simulated in 3D. At the end of the experiment of droplet motion, it gives a partial rebound outcome. As can be seen from the Fig. 16, a partial rebound outcome was achieved. As can be seen from Fig. 17, the droplet nondimensional spread factor was converged

.

CHAPTER IV

DROPLET IMPACTS ON SMOOTH MOVING WALL

In this section, experimental results and simulation results were compared in specific time sequences. The moving wall droplet simulations must be simulated in 3D due to the axisymmetry is broken. For this reason, 3D simulations are important for moving surface behaviors, which are the majority of drop-surface interactions in real life. It was necessary to solve problems such as squared droplet shapes due to the parasitic current effect in order for the 3-dimensional examinations to converge. Moving smooth surface simulations, different surface coating materials and their responses at the contact angles specified in the results are shown with physical image and non-dimensional spread factor. The ratio of the droplet inertia-surface tension relationship is characterized by non-dimentional We_n we We_t numbers for normal and tangential forces. In droplet experiments, attention has been paid to select the following simulation data in different regime map regions with We_n and We_t values. Comparative results for 3 different outcomes are shown with 7 selected simulations. Experimental data are generally compared with the 3D simulation results, and the simulations with the opportunity to compare the experimental data are compared with the spread factor chart and the instantaneous spread diameter values of the drop. As can be seen from the comparable figure, spreading and splashing processes are developed in accordance with the experiment. To better understand these processes, spread factor chart will help.

7 different experiment results were simulated under the conditions of the moving

wall ($We_t \neq 0$). Surface material, We_n and We_t values, Advancing , Receding, Equlibrium contact angle values are given in the Table 5. In order to compare the moving wall droplet simulation results with experimental data, it is necessary to compare the spread diameter of the asymmetric drop in the direction of the tangential and radial velocity vector separately. For this reason, 2 separate charts are presented for each simulation as tangetial and radial spread factor, which we do not see in static wall applications.FIG. 18 and FIG. 21 experimental results were compared with the 3D simulation results and their tangential FIG. 20, FIG. 23 FIG. 26 ,FIG. 29 and radial spread factor FIG. 19, FIG. 22, FIG. 25, FIG 28 data respectively. When comparing case7 tangential spread data, spread data begin to grow meaninglessly due to the shadow in the extraction of experimental data. We do not take the data results after the shadow growth begins as readable data. In case7, the results of the experiment in 2 different camera angle images with 27 were compared with the 3D simulation results. Case8 data selected from the [3] experiments matches the deposition droplet outcome on the regime map, case9 data matches the partial-rebound droplet outcome on the regime map, case10 data matches the split-deposition droplet outcome on the regime map. According to the results of first 3 cases, the tangential and radial spread factors data, which we have the opportunity to compare the spreading and deposition diameters of the drop on radial and tangential direction, and the results of the experiment and simulation converge. In addition to these, when the instantaneus figure of the drop is compared, the results of the static surface experiments and simulations converge. The last 4 experimental results are only presented with outcome matches because there is no experimental spread data.

Table 4: Number of grid cells and droplet diameter for moving wall cases.

Outcome	Experiment	Domain Size (mm)	No. of grid cells
Deposition	Kayansalcik [2]	1.6x2.8x5.5	3,723,654
Deposition	Kayansalcik [2]	1.6x2.8x5.5	3,723,654
Deposition	Kayansalcik [2]	1.6x2.8x5.5	3,723,654
Deposition	Kayansalcik [2]	1.5x2x9	2,652,502
Deposition	Chen&Wang [3]	1.5x2x12	2,651,688
Partial rebound	Chen&Wang [3]	1.5x2x12	2,651,688
Split Deposition	Chen&Wang [3]	0.8x2x9	5,361,190

Table 5: Impact conditions for the all validation cases

Case	Surf. Material	$\mathbf{We}_n$	$\mathbf{We}_t$	Drop. Size	θ_{adv}	θ_{rec}	θ_{eq}	*cAlpha*
4	Paraffin	42.3	14.49	0.75 (mm)	113°	63°	104°	0.24
5	Paraffin	51.41	16.54	0.86 (mm)	113°	63°	104°	0.24
6	Paraffin	81.5	16.26	0.84 (mm)	113°	63°	104°	0.24
7	Paraffin	19.04	14.57	0.76 (mm)	113°	63°	104°	0.28
8	Teflon	6.7	5.5	0.5 (mm)	142°	82°	103°	0.26
9	Teflon	39.8	0.3	0.5 (mm)	142°	82°	103°	0.26
10	Teflon	42.3	149	0.5 (mm)	142°	82°	103°	0.23

4.1 Results and Discussion

The tangential and radial spread factors data are given in all experimental cases, which we have the opportunity to compare the spreading and deposition diameters of the drop on radial and tangential direction. In moving wall applications, in addition to the radial spread factor, tangential spread factor definition and comparison are required. Tangential spread factor is defined with the ratio of initial drop diameter and instant spread diameter of drop on moving wall direction.

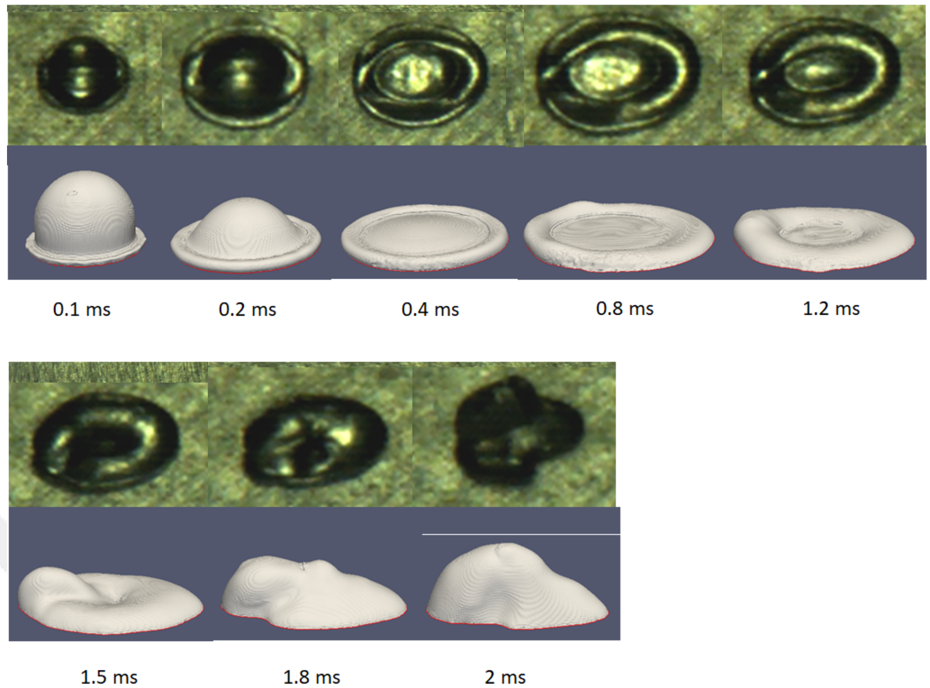

Figure 18: Time evolution of water drop impact on moving wax surface with deposition outcome. The wall moves to the right in the direction of the arrow (→). Simulated images are extracted from 3D simulation results (Case 4). Time slots are shown in milliseconds. Experimental images are taken from [2]

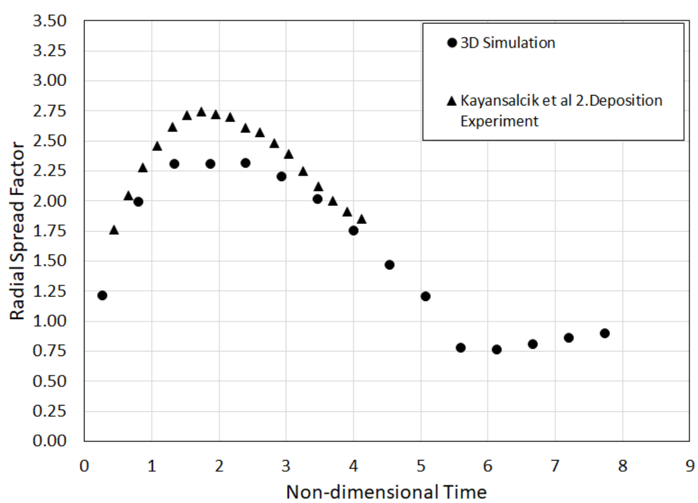

Figure 19: Non-dimensional radial spread factor versus non-dimensional time showing the evolution of the radial spread factor for reference deposition case (Case 4).

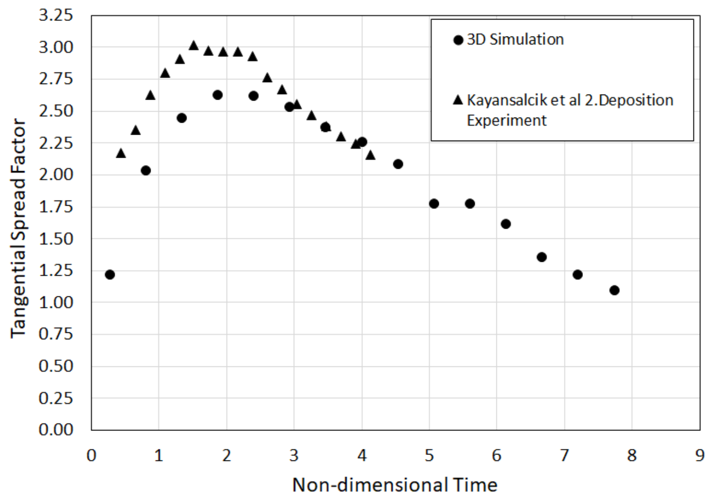

Figure 20: Non-dimensional tangential spread factor versus non-dimensional time showing the evolution of the tangential spread factor for reference deposition case (Case 4).

In Case 4 , the droplet impact on the moving paraffin surface was simulated in 3D. At the end of the experiment of droplet motion, it gives a deposition outcome. As can be seen from the Fig. 18, a deposition outcome was achieved. As can be seen from Fig. 19 and Fig. 20, the droplet nondimensional radial and tangential spread factor were converged. Experimental nondimensional spread factor datas cannot be used after a certain period of time. The reason for this is that the shadow created by the camera light on the droplet causes measurements as if the droplet diameter is enlarged after a certain period of time.

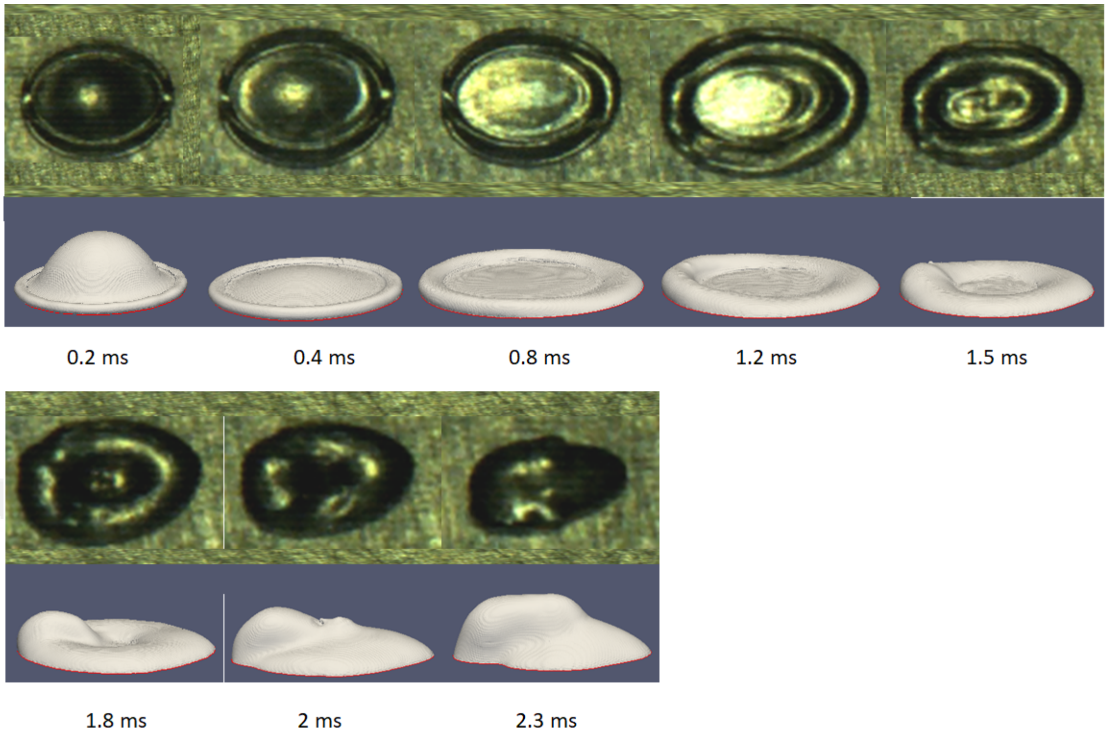

Figure 21: Time evolution of water drop impact on moving wax surface with deposition outcome. The wall moves to the right in the direction of the arrow (→). Simulated images are extracted from 3D simulation results (Case 5). Time slots are shown in milliseconds. Experimental images are taken from [2]

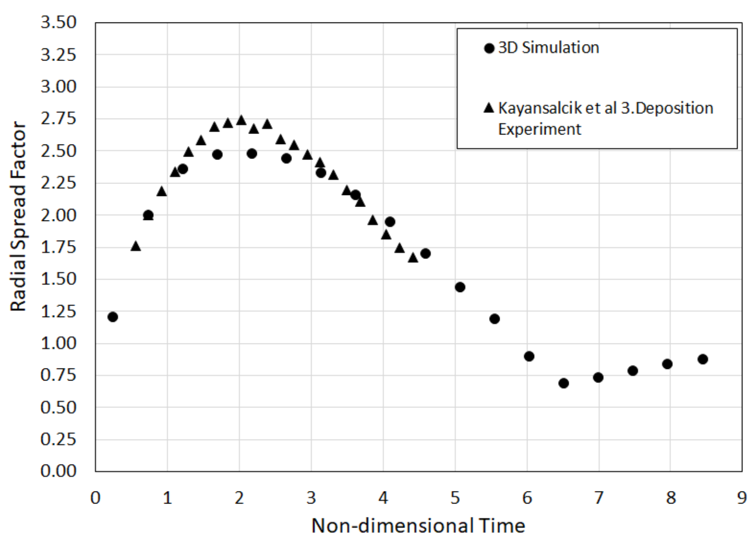

Figure 22: Non-dimensional radial spread factor versus non-dimensional time showing the evolution of the radial spread factor for reference deposition case (Case 5).

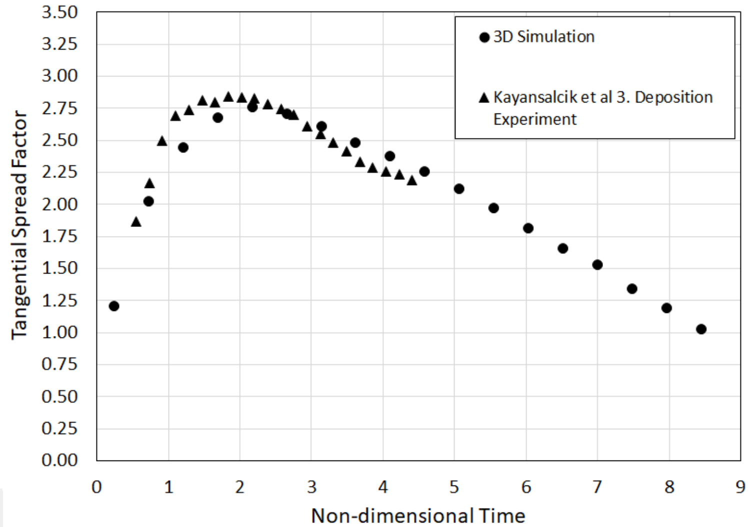

Figure 23: Non-dimensional tangential spread factor versus non-dimensional time showing the evolution of the tangential spread factor for reference deposition case (Case 5).

In Case 5, the droplet impact on the moving paraffin surface was simulated in 3D. At the end of the experiment of droplet motion, it gives a deposition outcome. As can be seen from Fig. 21, a deposition outcome was achieved. As can be seen from Fig. 22 and Fig 23, the droplet nondimensional radial and tangential spread factor were converged . Experimental nondimensional spread factor datas cannot be used after a certain period of time. The reason for this is that the shadow created by the camera light on the droplet causes measurements as if the droplet diameter is enlarged after a certain period of time.

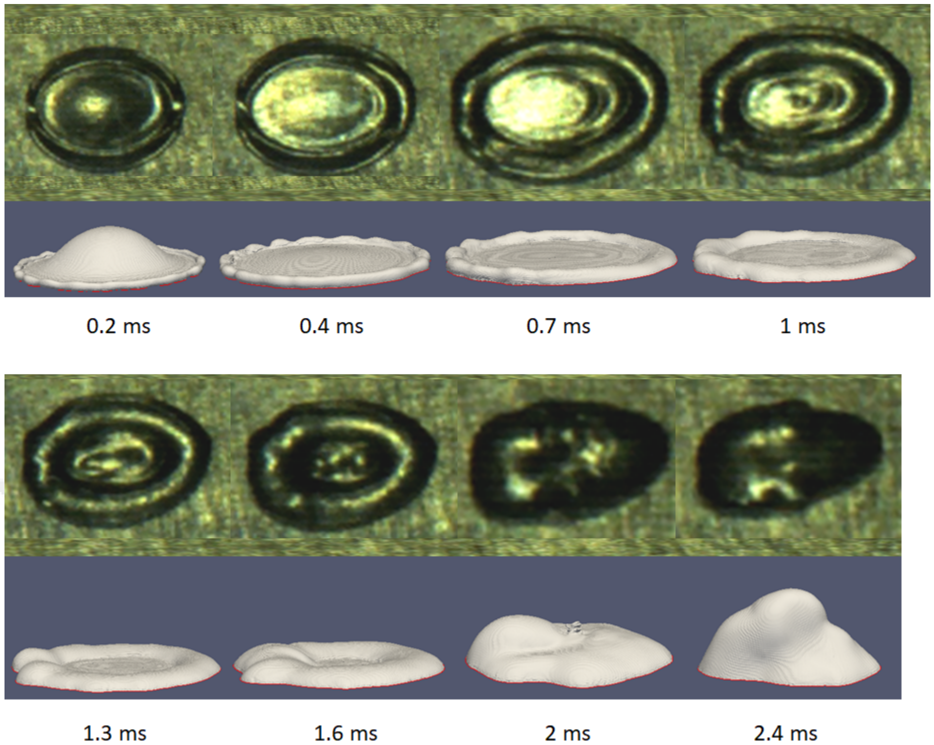

Figure 24: Time evolution of water drop impact on moving wax surface with deposition outcome. The wall moves to the right in the direction of the arrow (→). Simulated images are extracted from 3D simulation results (Case 6). Time slots are shown in milliseconds. Experimental images are taken from [2]

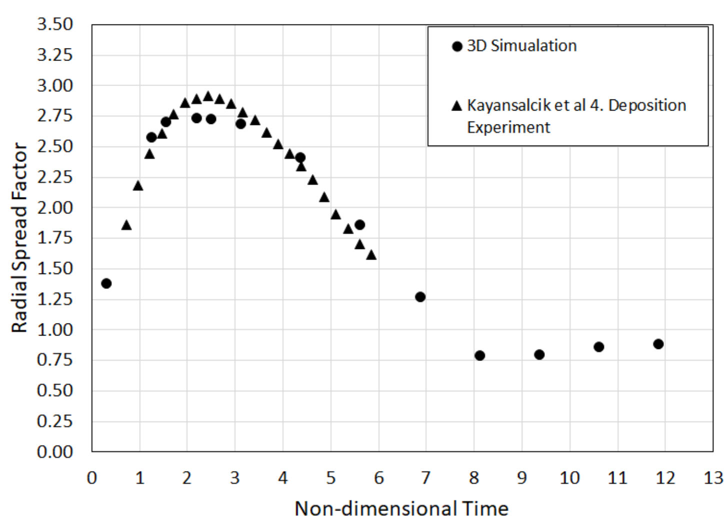

Figure 25: Non-dimensional radial spread factor versus non-dimensional time showing the evolution of the radial spread factor for reference deposition case (Case 6).

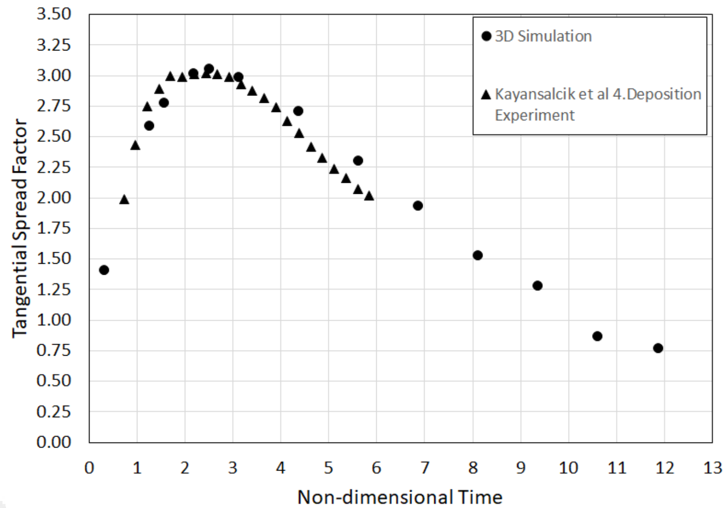

Figure 26: Non-dimensional tangential spread factor versus non-dimensional time showing the evolution of the tangential spread factor for reference deposition case (Case 6).

In Case 6, the droplet impact on the moving paraffin surface was simulated in 3D. At the end of the experiment of droplet motion, it gives a deposition outcome. As can be seen from the Fig. 24, a deposition outcome was achieved. As can be seen from Fig. 25 and Fig. 26, the droplet nondimensional radial and tangential spread factor were converged . Experimental nondimensional spread factor datas cannot be used after a certain period of time. The reason for this is that the shadow created by the camera light on the droplet causes measurements as if the droplet diameter is enlarged after a certain period of time.

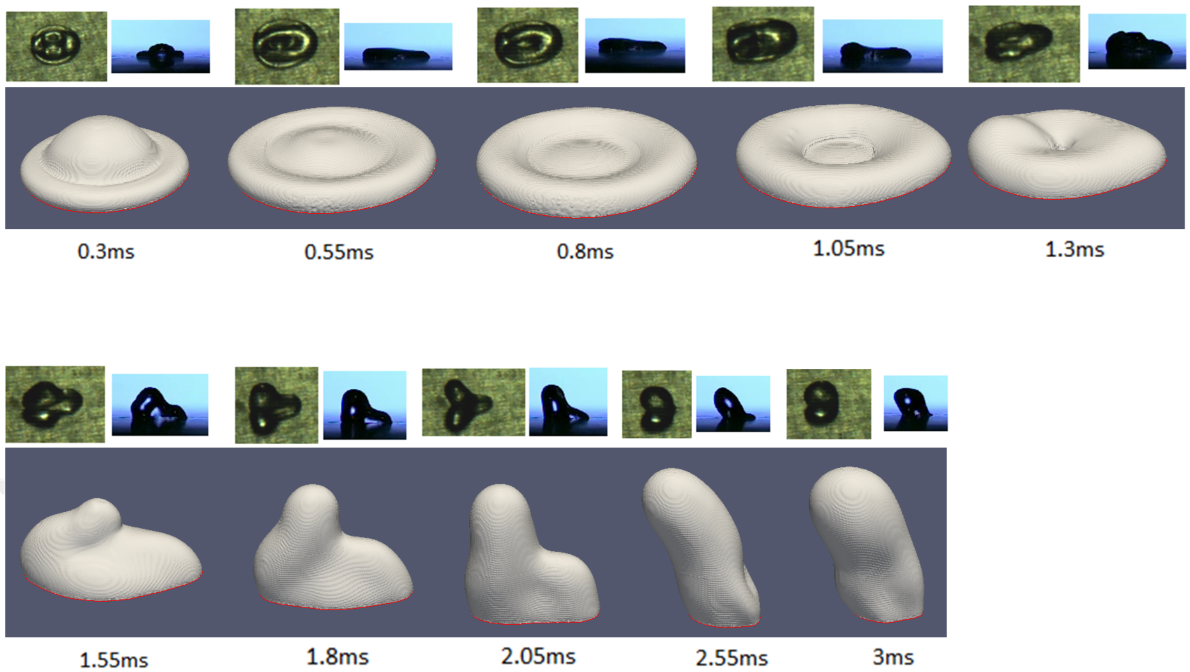

Figure 27: Time evolution of water drop impact on moving wax surface with deposition outcome. The wall moves to the right in the direction of the arrow (→) .Simulated images are extracted from 3D simulation results (Case 7). Time slots are shown in milliseconds. Experimental images are taken from [2]

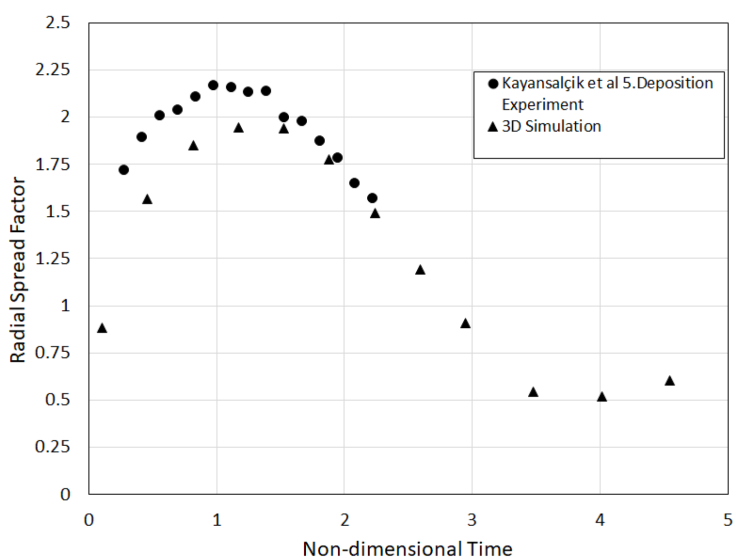

Figure 28: Non-dimensional radial spread factor versus non-dimensional time showing the evolution of the radial spread factor for reference deposition case (Case 7).

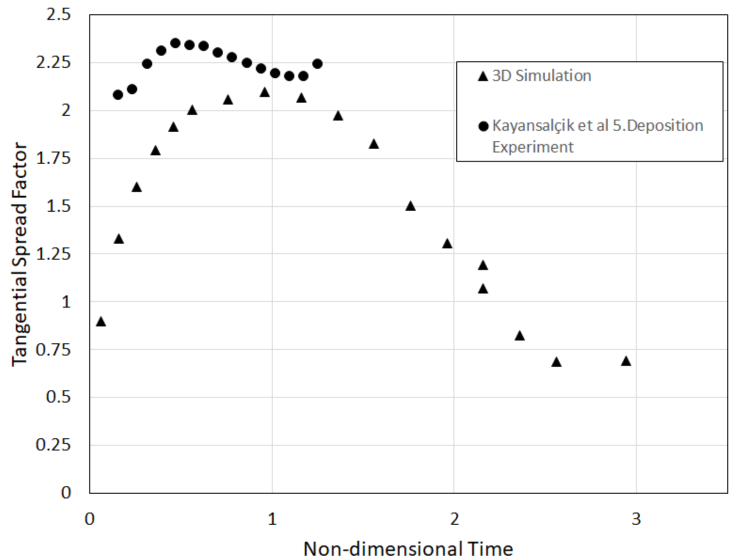

Figure 29: Non-dimensional tangential spread factor versus non-dimensional time showing the evolution of the tangential spread factor for reference deposition case (Case 7).

In Case 7, the droplet impact on the moving paraffin surface was simulated in 3D. At the end of the experiment of droplet motion, it gives a deposition outcome. As can be seen from Fig. 27, a deposition outcome was achieved. As can be seen from Fig. 28 and Fig. 29, the droplet nondimensional radial and tangential spread factor were converged . Experimental nondimensional spread factor datas cannot be used after a certain period of time. The reason for this is that the shadow created by the camera light on the droplet causes measurements as if the droplet diameter is enlarged after a certain period of time.

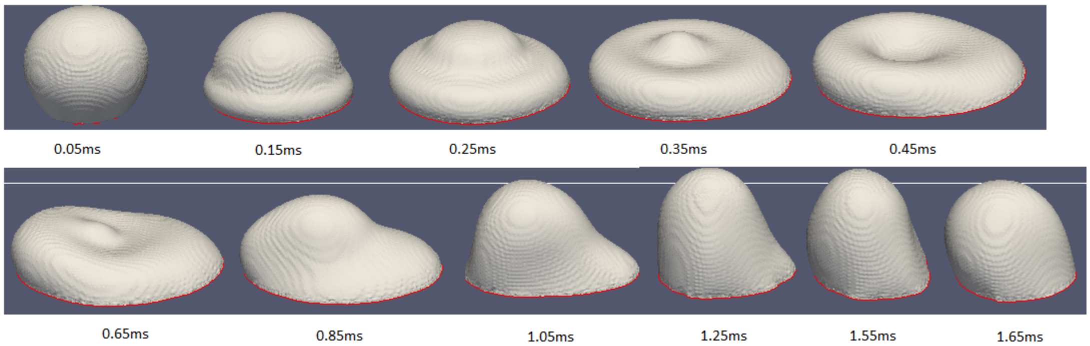

Figure 30: Time evolution of water drop impact on moving teflon surface with deposition outcome. The wall moves to the right in the direction of the arrow (→). Simulated images are extracted from 3D simulation results (Case 8). Time slots are shown in milliseconds.

In Case 8, the droplet impact on the moving teflon surface was simulated in 3D. The initial and surface conditions of this experimental data show that the drop will deposition outcome on the regime map. As can be seen from Fig. 30, a deposition outcome was achieved.

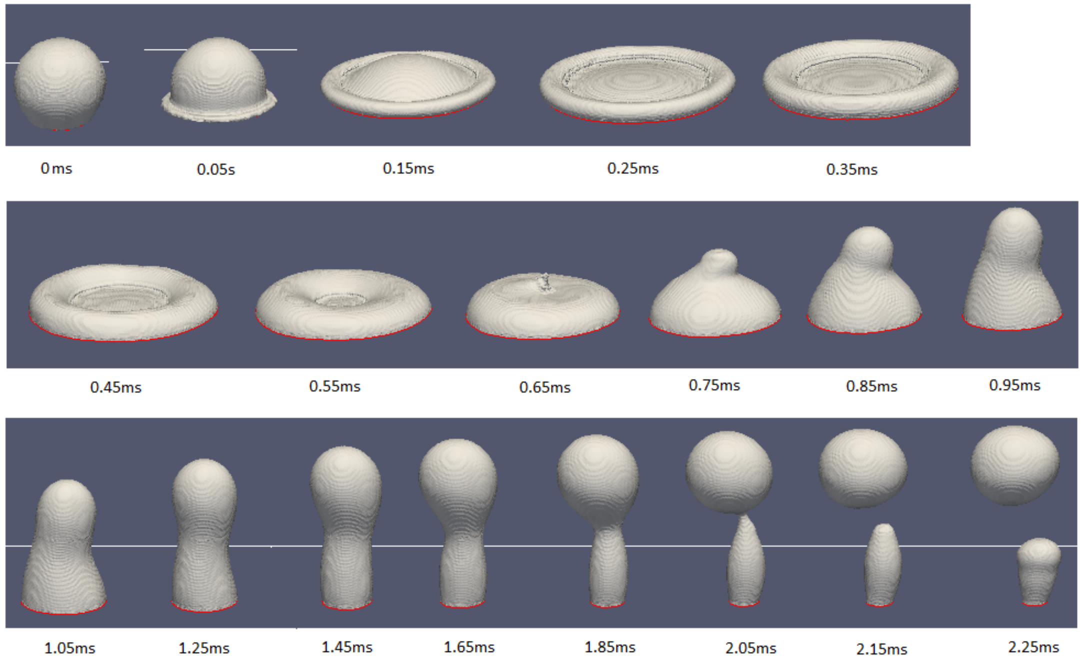

Figure 31: Time evolution of water drop impact on moving teflon surface with partial rebound outcome. The wall moves to the right in the direction of the arrow (→). Simulated images are extracted from 3D simulation results (Case 9). Time slots are shown in milliseconds.

In Case 9, the droplet impact on the moving teflon surface was simulated in 3D. The initial and surface conditions of this experimental data show that the drop will partial rebound outcome on the regime map. As can be seen from Fig. 31, a partial rebound outcome was achieved.

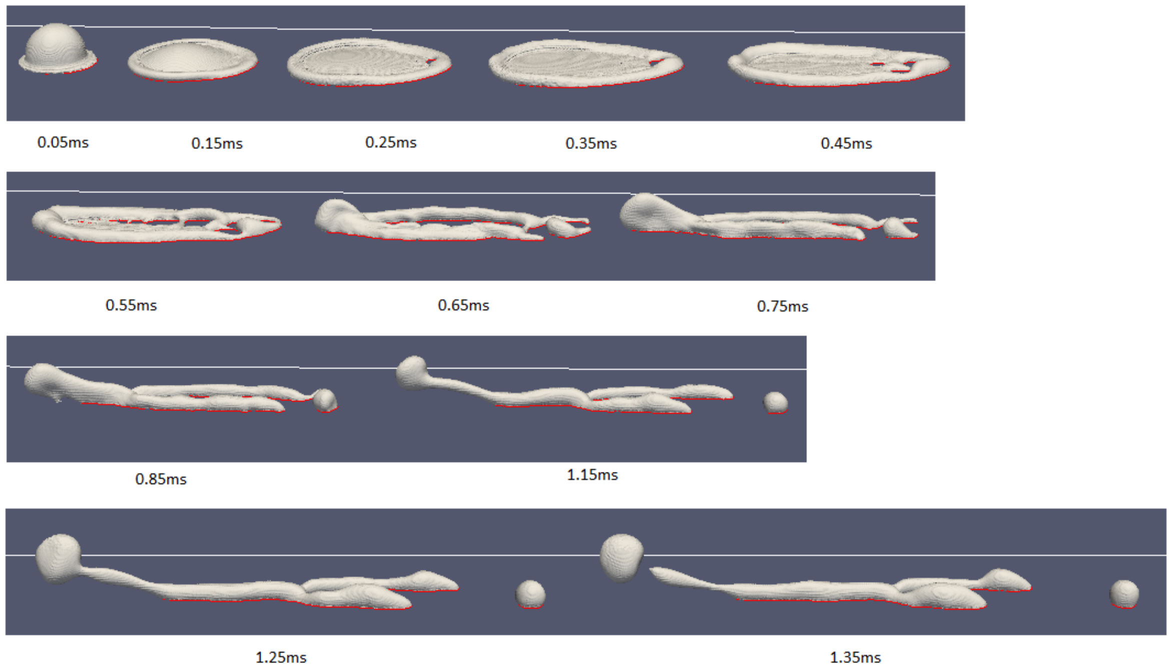

Figure 32: Time evolution of water drop impact on moving teflon surface with split deposition outcome. The wall moves to the right in the direction of the arrow ($\rightarrow$). Simulated images are extracted from 3D simulation results (Case 10). Time slots are shown in milliseconds.

In Case 10, the droplet impact on the moving teflon surface was simulated in 3D. The initial and surface conditions of this experimental data show that the drop will split deposition outcome on the regime map. As can be seen from Fig. 32, a split deposition outcome was achieved.

CHAPTER V

CONCLUSION

In this study, it is aimed to simulate droplet simulations in having different droplet impact outcomes with acceptable accuracy in transient evolution of their shape. For this purpose, first the error cause of parasitic current is investigated. It is found that there was a correlation between parasitic current and mesh distribution on spreading plane. The source of this correlation comes from gradient calculations that directly effect parasitic current. It is shown that, the parasitic current generation cannot be decreased by increasing the mesh refinement in the framework of CSF where the generation of parasitic currents originates from use of volume fraction gradients at the droplet interface. When the parasitic current and interface deformation were examined, it was observed that the errors accumulate in the spreading plane. By increasing the number of neighboring cells of the grid in this plane, the gradient errors have attained lower amplitudes with higher frequencies. Hence, increasing the number of neighbors for each cell in the propagation plane by using polygonal cells, the smoother distribution of the volume fraction gradients and the reduction of the cummulative error to acceptable levels are achieved. After implementing the modified Kistler model to predict the instantaneous contact angle and using a polygonal mesh structure, without any further intervention in the simulations correct evolution of the droplet shapes could be captured.

For the validation cases, we especially get data of different impact outcomes for statinary and moving wall conditions. Comparably good results were produced for 10 experimental test cases with a normal Weber number less than 100. However, validation with experimental cases with high normal Weber number ($We_n > 100$)

was not possible because of the computational cost. This study suggests that AMR method should be made for polyhedral cell structure in order to reduce computational time while decreasing the parasitic currents, so that simulations with higher weber Numbers becomes possible. In addition, parasitic current generation can be reduced by a model in which the gradient computation scheme involve information from higher number of neighboring cells.

5.1 Future Work

For future studies, the development of computational equipment and software should be followed and the interactions of the droplet with the surface at high velocity should be simulated. Adaptive Mesh Refinement codes should be applied on polyhedral grid to increase the stability in simulations. In addition, for gradient calculations, it is possible to model with gaussian method with increased number of neighboring edges, reducing gradient fluctuations and thus parasitic current effects.

APPENDIX A

SOME ANCILLARY STUFF

A.1 Matlab codes to calculate gradient values on cartesian and polyhedral grid structure

These codes are written to gradient calculations in Cartesian and Polyhedral grid structure. Gauss green method is used in gradient calculations.

These codes are available on github website below.

https://github.com/ANILYILLMAZ/Cartesian-Polyhedral-Gauss-Green-Gradient-Calculator

A.2 OpenFOAM numerical schemes

```
ddtSchemes
{
    default CrankNicolson 0.8
        ddt(phi) CrankNicolson 0.8;
}

gradSchemes
{
    default          Gauss linear;
    grad(U)          Gauss linear;
    grad(alpha)      Gauss cubic ;
}

divSchemes
{
    div(rhoPhi,U)  Gauss linearUpwind grad(U);
    div(phi,alpha)  Gauss linear;
    div(phirb,alpha) Gauss linear;
```

Figure 33: Numerical methods (../system/fvSchemes) in openFoam

A.3 OpenFOAM on HPC cluster

```
[ayilmaz@headnode movwall ]$ spart
         QUEU STA   FREE  TOTAL RESORC  OTHER   FREE  TOTAL ||   NODE
     PARTITIO TUS  CORES  CORES PENDNG PENDNG  NODES  NODES || MEM-GB
         defq   *    173    196      0      0      4      7 ||    120
         gpuq         56     56      0      0      2      2 ||    250
        mqall        240    280      0      0      6     10 ||    120
       serial         51     84      0      0      0      3 ||    120
test-OSupdate         35     56      0      0      0      2 ||    120

                  YOUR PEND PEND YOUR   MIN  CORES
                   RUN  RES OTHR TOTL NODES  /NODE
   COMMON VALUES:    0    0    0    0     1     28
[ayilmaz@headnode movwall ]$ sinfo -l -lNe
Sat Dec 19 15:30:43 2020
NODELIST   NODES      PARTITION       STATE CPUS    S:C:T MEMORY TMP_DISK WEIGHT AVAIL_FE REASON
cnode001       1          mqall        idle   28   2:14:1 250000        0      1   (null) none
cnode001       1           gpuq        idle   28   2:14:1 250000        0      1   (null) none
cnode002       1          mqall        idle   28   2:14:1 250000        0      1   (null) none
cnode002       1           gpuq        idle   28   2:14:1 250000        0      1   (null) none
cnode003       1          defq*        idle   28   2:14:1 250000        0      1   (null) none
cnode003       1          mqall        idle   28   2:14:1 250000        0      1   (null) none
cnode004       1          defq*       mixed   28   2:14:1 250000        0      1   (null) none
cnode004       1          mqall       mixed   28   2:14:1 250000        0      1   (null) none
cnode005       1          defq*        idle   28   2:14:1 250000        0      1   (null) none
cnode005       1          mqall        idle   28   2:14:1 250000        0      1   (null) none
cnode006       1          defq*       mixed   28   2:14:1 250000        0      1   (null) none
cnode006       1          mqall       mixed   28   2:14:1 250000        0      1   (null) none
cnode007       1          defq*        idle   28   2:14:1 250000        0      1   (null) none
cnode007       1          mqall        idle   28   2:14:1 250000        0      1   (null) none
cnode008       1          defq*        idle   28   2:14:1 250000        0      1   (null) none
cnode008       1          mqall        idle   28   2:14:1 250000        0      1   (null) none
cnode009       1          defq*       mixed   28   2:14:1 120000        0      1   (null) none
cnode009       1          mqall       mixed   28   2:14:1 120000        0      1   (null) none
cnode010       1         serial       mixed   28   2:14:1 120000        0      1   (null) none
cnode011       1         serial       mixed   28   2:14:1 120000        0      1   (null) none
cnode011       1 test-OSupdate        mixed   28   2:14:1 120000        0      1   (null) none
cnode012       1         serial       mixed   28   2:14:1 120000        0      1   (null) none
cnode012       1 test-OSupdate        mixed   28   2:14:1 120000        0      1   (null) none
cnode012       1          mqall       mixed   28   2:14:1 120000        0      1   (null) none
[ayilmaz@headnode movwall ]$
```

Figure 34: Capacity of HPC Cluster

The simulation file is shown schematically in the figure below.

```
[ayilmaz@headnode movwall ]$ ls
0  constant  openfoam-run.sh  system
```

Figure 35: Simulation case on Slurm

"sbatch" submits a batch script to Slurm. The simulation specified with the batch script content is queued for parallel calculations with the written node or processor numbers.The content of parallel script (.sh) created for myinterFoam executable is given below.

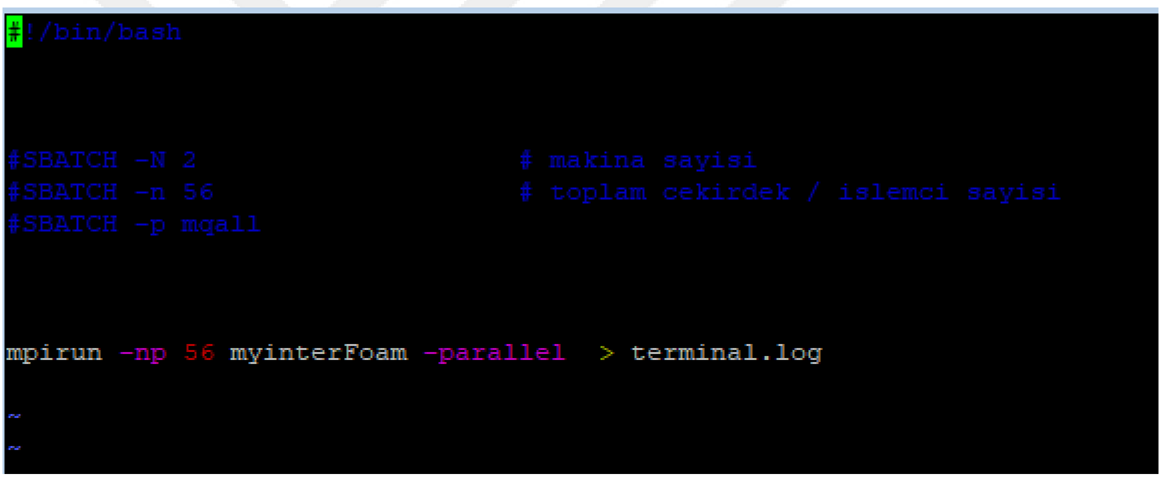

Figure 36: Batch Script (.sh) of myinterFoam on Slurm

Bibliography

[1] R. Rioboo, M. Marengo, and C. Tropea, "Time evolution of liquid drop impact onto solid , dry surfaces," *Experiments in Fluids*, vol. 33, no. October 2014, pp. 112–124, 2002.

[2] G. Kayansalcik, "Experimental Investigation Of Droplet Impact On Moving Surfaces Experimental Investigation Of Droplet," Master's thesis, Özyeğin University, 2018.

[3] R. Chen and H. Wang, "Effects of tangential speed on low-normal-speed liquid drop impact on a non-wettable solid surface," *Experiments in Fluids*, vol. 39, pp. 754–760, 2005.

[4] K. Vontas, M. Andredaki, A. Georgoulas, K. S. Nikas, and M. Marengo, "Numerical Investigation of Droplet Impact on Smooth Surfaces with Different Wettability Characteristics: Implementation of a dynamic contact angle treatment in OpenFOAM.," *Proceedings ILASS–Europe 2017. 28th Conference on Liquid Atomization and Spray Systems*, no. September, 2017.

[5] S. Wildeman, C. W. Visser, C. Sun, and D. Lohse, "On the spreading of impacting drops," *Journal of Fluid Mechanics*, vol. 805, pp. 636–655, 2016.

[6] Z. Jian, C. Josserand, S. Popinet, P. Ray, and S. Zaleski, "Two mechanisms of droplet splashing on a solid substrate," *Journal of Fluid Mechanics*, vol. 835, pp. 1065–1086, 2018.

[7] C. W. Extrand and Y. Kumagai, "Liquid drops on an inclined plane: The relation between contact angles, drop shape, and retentive force," *Journal of Colloid and Interface Science*, vol. 170, no. 2, pp. 515 – 521, 1995.

[8] D. J. E. Harvie, M. R. Davidson, and M. Rudman, "An analysis of parasitic current generation in Volume of Fluid simulations," *Applied Mathematical Modelling*, vol. 30, pp. 1056–1066, 2006.

[9] J. U. Brackbill, D. B. Kothe, and O. Ridge, "A Continuum Method for Modeling Surface Tension A Continuum Method for Modeling Surface Tension *," *Journal of Computational Physics*, vol. 9991, no. November 2017, 1992.

[10] M. Berger and P. Colella, "Local Adaptive Mesh Refinement for Shock Hydrodynamics," *Journal of Computational Physics*, vol. 82, pp. 64–84, 1989.

[11] S. Popinet, "Gerris : a tree-based adaptive solver for the incompressible Euler equations in complex geometries," *Journal of Computational Physics*, vol. 190, pp. 572–600, 2003.

[12] S. Popinet, "A quadtree-adaptive multigrid solver for the Serre – Green – Naghdi equations," *Journal of Computational Physics*, vol. 302, pp. 336–358, 2015.

[13] S. Afkhami and M. Bussmann, "Height functions for applying contact angles to 3D VOF simulations," *International Journal for Numerical Methods in Fluids*, vol. 57, pp. 453–472, 2008.

[14] S. Osher and James A. Sethian, "Fronts Propagating with Curvature Dependent Speed: Algorithms Based on Hamilton-Jacobi Formulations," *Journal of Computational Physics*, vol. 79, pp. 12–49, 1988.

[15] C. Hirt and B. Nichols, "Volume of Fluid (VOF) Method for the Dynamics of Free Boundaries," *Journal of Computational Physics*, vol. 39, pp. 201–255, 1981.

[16] K. Eisenschmidt, M. Ertl, H. Gomaa, C. Kieffer-roth, C. Meister, P. Rauschenberger, M. Reitzle, K. Schlottke, and B. Weigand, "Direct numerical simulations for multiphase flows : An overview of the multiphase code FS3D," *Applied Mathematics and Computation*, vol. 272, pp. 508–517, 2016.

[17] M. Boger, J. Schlottke, and B. Weigand, "Reduction of parasitic currents in the DNS VOF code FS3D." 2010.

[18] F. Denner, F. Evrard, R. Serfaty, and B. G. M. V. Wachem, "Artificial viscosity model to mitigate numerical artefacts at fluid interfaces with surface tension," *Computers and Fluids*, vol. 143, pp. 59–72, 2017.

[19] Z. Pan, "Spurious Current Suppression in VOF-CSF Simulation of Slug Flow through Small Channels." 2015.

[20] K. Yokoi, D. Vadillo, J. Hinch, and I. Hutchings, "Numerical studies of the influence of the dynamic contact angle on a droplet impacting on a dry surface," *Physics of Fluids*, 2009.

[21] S. Kistler, *Hydrodynamics of Wetting, in Wettability, Surfactant Science Series 49, 311-429.ed. J.C. Berg, New York, NY, Marcel Dekker*. 1993.

[22] H. Heidarifatasmi and O. Ertunç, "Simulations of droplet impacts on hydrophobic moving walls." Droplet 2017, 7 2017. UCLA, Los Angeles.

[23] H. Heidarifatasmi, "Simulations of Droplet Impacts on Hydrophobic Moving Walls," Master's thesis, Ozyegin University, 2017.

[24] J. Eggers, M. A. Fontelos, C. Josserand, and S. Zaleski, "Drop dynamics after impact on a solid wall: Theory and simulations," *Phys. Fluids*, vol. 22, no. 6, pp. 62101–62113, 2010.

[25] C. Josserand, P. Ray, and S. Zaleski, "Droplet impact on a thin liquid film: Anatomy of the splash," *Journal of Fluid Mechanics*, vol. 802, pp. 775–805, 2016.

[26] C. Josserand, P. Ray, and S. Zaleski, "Air entrapment and splashing treshold in drop impacts," *7th International Conference on Multiphase Flow, ICMF 2010*, no. 2003, pp. 1–7, 2010.

[27] Y. Guo, L. Wei, G. Liang, and S. Shen, "Simulation of droplet impact on liquid film with CLSVOF," *International Communications in Heat and Mass Transfer*, vol. 53, pp. 26–33, 2014.

[28] J. Philippi, A. Antkowiak, and P. Y. Lagrée, "A pressure impulse theory for hemispherical liquid impact problems," *European Journal of Mechanics, B/Fluids*, 2018.

[29] E. Berberovic, "Evaluation of the dynamic contact angle using the hoffman function, based on kistler (1993)," no. November, 2008.

[30] H. G. Weller, G. Tabor, H. Jasak, and C. Fureby, "techniques A tensorial approach to computational continuum mechanics using object-oriented techniques," *Computers in Physics*, vol. 620, no. 1998, 1999.

[31] A. Afshar, D. Version, and A. Afshar, *Numerical Wave Generation In OpenFOAM R Master of Science Thesis Department of Shipping and Marine Technology*. PhD thesis, 2010.

[32] R. L. Hoffman, "A study of the advancing interface. i. interface shape in liquid—gas systems," *Journal of Colloid and Interface Science*, vol. 50, no. 2, pp. 228 – 241, 1975.

[33] N. Linder, A. Criscione, I. V. Roisman, H. Marschall, and C. Tropea, "3D computation of an incipient motion of a sessile drop on a rigid surface with contact angle hysteresis," *Theor. Comput. Fluid Dyn.*, 2015.

[34] Siemens PLM Software, "Simcenter star-ccm+® documentation version 13.06 user manual," 2018.

[35] J. Crank and P. Nicolson, "A practical method for numerical evaluation of solutions of partial differential equations of the heat-conduction type," *Mathematical Proceedings of the Cambridge Philosophical Society*, vol. 43, no. 1, p. 50–67, 1947.

[36] J. Ferziger and M. Peric, *Computational Mehhods for Fluid Dynamics*. Springer, 3.rd ed., 2002.

[37] R. Issa, "Solution of the implicitly discretised fluid flow equations by operator-splitting," *Journal of Computational Physics*, vol. 62, no. 1, pp. 40 – 65, 1986.

VITA

Anıl Yılmaz received the B.Sc. degree in Mechanical Engineering from Kocaeli University, Kocaeli, Turkey in 2016 and he is currently pursuing the M.Sc. degree in Mechanical Engineering at Ozyegin University. His field of research are multiphase flow simulations and matematical modelling.